Low Frequency and Total Internal Reflection Raman Spectroscopic Study of Ions in Bulk and at the Silica/Aqueous Interface

THESIS

Presented in Partial Fulfillment of the Requirements for the Degree Master of Science in the Graduate School of The Ohio State University

By

Xiao Shou, B.A.

Graduate Program in Chemistry

The Ohio State University

2014

Master's Examination Committee:

Prof. Dr. Heather C. Allen, Advisor

Prof. Dr. James V. Coe

Abstract

In this study, ion-specific effects were examined by Raman spectroscopic techniques through the interaction with water in the bulk and that at the silica/aqueous interface. In the bulk, cation-water interactions are characterized by metal-water and hydrogen bond stretch vibrations in the low frequency region. Mg^{2+} interacts with water more strongly than Ca^{2+} as shown by the more intense and higher frequency Mg-O stretch at ~355 cm^{-1} compared to the Ca-O stretch at ~320 cm^{-1}. Anions play a major role by perturbing the hydrogen bonding network of water. The hydrogen bond stretch was determined to be around ~ 230 cm^{-1} depending on the anion. Perchlorate and sulfate were found to perturb the water structure more significantly as indicated by the blue shift of the hydrogen bond stretch, whereas chloride and nitrate did not have such a pronounced effect. Divalent cations studied here Mg^{2+} and Ca^{2+} were shown to have a smaller effect on the hydrogen bonded network of water, even though their interactions with water are fairly different.

Adsorption processes at the silica/aqueous interfaces are dictated by electrostatic interactions which involve the transfer of protons from surface silanol sites to oxyanions. This interfacial behavior is captured by total internal reflection (TIR)-Raman spectroscopy. The interfacial pHs of several oxyanion solutions were extracted from spectral information using the Henderson-Hasselbach approximation; NO_3^- (-0.2 ± 0.1) ≈

ClO_4^- (0.0 ± 0.3) < SO_4^{2-} (3.2 ± 0.6). These interfacial pH values differ significantly from the bulk pH (2.0 ± 0.2). The non-protonated oxyanion symmetric mode was largely enhanced by addition of background electrolytes due to (1) increased Raman transition strength (2) charge screening shifted chemical equilibrium of (de)protonation toward oxyanion formation direction and (3) electrical double layer moving closer to the surface where the electric field is strongest.

Dedication

This thesis is dedicated to my family and friends.

Acknowledgments

In the writing of this thesis I would like to thank various members in the Allen Research Laboratory at the Ohio State University. First and foremost, I would like to express my thankfulness and appreciation to my advisor Dr. Heather C. Allen for her help, advice, motivation, and support in graduate level study and research. I am still very grateful to her for she gave me a second chance to complete this degree. I would also like to thank my fellow colleagues in the Allen Lab, in particular Dr. Dominique Verreault for his generous help in discussing research related issues, and writing this thesis. I would also like to thank my colleague Mr. Brant M. Finzer for working together with me in setting up of low frequency, conventional and TIR Raman instruments. In addition, I am grateful to my host family, Matt and Kristin Cline for helping to get settled here in Columbus, Ohio, and my friend Mr. Jiayi Liu to train with me and be supportive during my graduate life. A special thanks to Professor Xuenian Chen, for his career advice and offer of a potential job. And finally to my family especially my mother for giving me the strength and courage to pursue a higher education and for all their love and support.

Vita

January 6th, 1990 ..... Born – Shanghai, China

2008 – 2012 ..... B.A. Chemistry, Wittenberg University, Springfield, Ohio, USA

2012 – 2013 ..... Graduate Teaching Associate, Department of Chemistry and Biochemistry, The Ohio State University – Columbus, Ohio, USA

2013 – Present ..... Graduate Research Associate, Department of Chemistry and Biochemistry, The Ohio State University – Columbus, Ohio, USA

Field of Study

Major Field: Chemistry

Table of Contents

List of Figures

List of Tables

List of Abbreviations and Symbols

Abbreviations

ATR	attenuated total reflection
BD	beam dump
CCD	charge-coupled device
CIP	contact ion pair
EM	electromagnetic
FL	focusing lens
FWHM	full width at half maximum
HP	hemispherical prism
IR	infrared
LPF	longpass filter
TIR	total internal reflection
WSR	water-to-salt ratio
MD	molecular dynamics
VSFG	vibration sum frequency generation

Symbols

α	polarizability
ε_0	electric constant
ε_r	relative static permittivity
λ	wavelength
λ_0	excitation wavelength
θ_i	incident angle
θ_c	critical angle
ω	frequency
$\Delta\omega$	Raman shift
c	speed of light
d_p	penetration depth
e	elementary charge
β	decay coefficient
$\mathbf{E}$	electric field
$\mathbf{E}_0$	amplitude (vectorial) of the electric field
$\mathbf{E}_i$	electric field of the incident wave
$\mathbf{E}_r$	electric field of the reflected wave
$\mathbf{E}_t$	electric field of the transmitted wave
$\mathbf{k}$	wave vector
k_B	Boltzmann constant
$\mathbf{k}_i$	wave vector of the incident wave
$\mathbf{k}_r$	wave vector of the reflected wave
$\mathbf{k}_t$	wave vector of the transmitted wave
K_a	acid disociation constant

$M_{vv'}$	Raman transition moment integral
n	refractive index
n_i	refractive index of the incident medium
n_j	bulk concentration of the j^{th} species in the solution
n_t	refractive index of the transmitted medium
$r_{M\text{-}O}$	metal-oxygen distance in the first hydration shell of hydrated systems
r^p	*p*-polarized Fresnel reflection coefficient
r^s	*s*-polarized Fresnel reflection coefficient
R_p	*p*-polarized reflectance
R_s	*s*-polarized reflectance
t	time
T	temperature
t_{px}	*p*-polarized Fresnel transmission coefficient in *x*-axis
t_{sy}	*s*-polarized Fresnel transmission coefficient in *y*-axis
t_{pz}	*p*-polarized Fresnel transmission coefficient in *z*-axis
ν	vibrational mode
z	electric charge

Chapter 1

Introduction

The original Hofmeister series, below, takes its shape in the ranking of various anions and cations toward their ability to precipitate a mixture of hen egg white proteins.[1] The so-called "salt-in" and "salt-out" effects are specifically associated with these simple ions. Ions in general are particularly interesting to investigate not only due to their abundance in nature, but also because of the roles they play in different scientific fields.

Anions:

$$\text{citrate}^{3-} > SO_4^{2-} = \text{tartrate}^{2-} > HPO_4^{2-} > CrO_4^{2-} > \text{acetate}^{-} > HCO_3^{-} > Cl^{-} > NO_3^{-} > ClO_3^{-}$$

Cations:

$$Mg^{2+} > Li^{+} > Na^{+} = K^{+} > NH_4^{+}$$

Simple cations such as Mg^{2+}, Ca^{2+}, and Na^{+} are rich in natural water systems such as oceans. Mg^{2+} and Ca^{2+} are the two most abundant divalent ions in seawater, and they are crucial to the oceanic aerosol formation which is related to climate change.[2] They also play an important role in biological activities such as stabilization of nucleic acids and enzyme catalysis because they are readily available to cells.[3-5] Divalent cations such as

Mg^{2+} and Ca^{2+} especially, participate in charge development at surfaces and interfaces, and interact with soft matter such as lipid membranes, which alters their behavior and functionality.[6, 7] However, due to their different interaction with water, as will be discussed later in this study, the chemistry and biochemistry differ significantly. For example, the transport of these coordinated ions in cells are different due to the size of hydrated radii; the binding with multivalent ligands differ due to the binding strength with the coordinated water.[8] The dynamics of the interaction between the two cations and biomolecules in cell are thus fairly distinguishable from each other.

Polyatomic anions, particularly oxyanions, on the other hand, impact significantly the chemistry of atmosphere and oceans. Oxyanions such as nitrate (NO_3^-) and sulfate (SO_4^{2-}) are the two main components of atmospheric aerosols. In the stratosphere chemistry, sulfate and nitrate are two sources of acid rain. They originate from oxidation of SO_2 and NO_2 and are deposited to the Earth surface by dry or wet deposition.[9] Nitrate and sulfate are the main components of stratospheric aerosols which have received much attention in the past because they are involved in heterogeneous reactions toward ozone depletion processes.[10] A good example is the formation of catalytically active Cl in the reaction of hydrogen chloride (HCl) and chlorine nitrate ($ClONO_2$), which only occurs on catalytic surfaces of particular matter of nitrate and sulfate.[11] Similarly, perchlorate (ClO_4^-), a proved iodide uptake inhibitor has been readily found in many rain and snow samples. It is usually formed from electrical discharging chloride aerosol and by exposing aqueous chloride to high concentrations of ozone.[12] In recent years, perchlorate has been found in ground water systems particularly in the southwestern area of the U.S.

as an environmental pollutant possibly due to the industrial uses as rocket propellants, explosives and automobile air bag systems.[12]

The study of ions and their specific effects in biological and chemical processes in solution and sometimes at interfaces provides some insight into the understanding of naturally occurring phenomena and practical problems in our everyday life. The goal of this project is to shed some light on the interaction of divalent ions Mg^{2+} and Ca^{2+}, oxyanions (NO_3^-, SO_4^{2-} , ClO_4^-,), and halides such as Cl^-, with water in the bulk and at the silica surface.

Chapter 2

Low Frequency Vibrations in Bulk Aqueous Solutions

2.1 Introduction
2.1.1 Ion−Water Interaction

Various phenomena in nature regarding ion-specific effects occur in aqueous solution. The activities of divalent cations such as their transport across biological membranes usually involve hydrated forms of these ions. It is thought by some that the nature of hydration is mainly an ion-dipole interaction because the main contributing force is electrostatic, although in some cases, the metal−water bond is found partially covalent.[13] In general, this type of interaction strongly depends on charge density, along with other factors such as size, polarizability and geometry.[14] Mg^{2+} for example will certainly interact more strongly with water than Ca^{2+} and Sr^{2+} because of its high charge density. The hydration properties of metal salts in an aqueous environment and their hydrated form have been studied extensively in the last decade both experimentally and computationally; most of these studies have been reviewed by Marcus and others.[15-17] The main aspects of these studies have been focused on the geometry of the hydrated systems, $M-O_w$ distance coordination number of first and second hydration shells by methods such as X-ray and neutron diffraction, infrared and Raman spectroscopy and

MD simulations. These studies reveal that the Mg−O bond length is significantly shorter than the Ca−O and Na−O bonds, both in their crystal structure and in aqueous solution.[18-41] The coordination number of magnesium and sodium systems is confirmed to be 6, while the calcium hydrated system tends to vary; in some cases, it is concentration- and anion-dependent.[42] In the solvated magnesium carbonate and bicarbonate complexes, for example, Mg^{2+} is mostly five-coordinated, not octahedrally coordinated, according to Di Tommaso et al.[43] Kapitan et al. computationally determined the bond length between the metal cation and oxygen from water in the first hydration shell (r_{M-O}) of the following three systems assuming an octahedral geometry: $[Mg(H_2O)_6]^{2+}$: 2.0−2.1Å, $[Ca(H_2O)_6]^{2+}$: 2.4−2.6 Å, $[Na(H_2O)_6]^{2+}$: 2.3−2.4 Å.[13] The variation of bond length certainly has an impact on the vibrational frequency of different hydrated metal systems. Kanno was able to find a simple linear relation derived from the Born equation and linear harmonic oscillator model between divalent metal M^{2+}−O_w vibration ν_1 and $1/r_{M-O}^2$.[44] This provides a reasonable explanation for the shifts in the vibrational modes of M−O stretch, because as bond length increases, the vibration strength will be significantly weakened causing a red shifted of its peak frequency. Hawlicka et al., on the other hand, simulated the interaction energy of the three different systems, Mg^{2+} … OH_2 , Ca^{2+} … OH_2, and Na^+ … OH_2 and considered Mg^{2+} … OH_2 as the most energetically favored, then Ca^{2+} and Na^+.[42] This study also confirms the oscillation strength are in the order of Mg-O_w > Ca^{2+} -O_w > Na^+-O_w hydrated systems, which is rather consistent with other studies.

Concentration or water-to-salt ratio (WSR), as mentioned above is a key parameter that governs the hydration properties of metal salts. Although anion solvation is much

less studied due to the fact that anion-water interaction is weaker compared to the cation-water one, the role that the anion in aqueous system is of equal importance because of ion pairing at different concentrations. Three types of ion pairing may be considered: solvent-separated ion pairs where the solvation shell for both cations and anions are intact, solvent-shared ion pairs where the solvation shell is shared by cations and anions, and contact ion pairs (CIPs) where ions are directly in contact predominately due to electrostatic attraction. CIP formation is essentially an ion-ion interaction. In aqueous environment, ion-dipole interactions compete with ion-ion interactions: the more solvent is available, the less likely solute ions can contact electrostatically. Usually, CIP formation takes place at fairly high concentrations for two species with high charge density. Thus at high concentrations, CIPs have to be taken into consideration. Mg^{2+}−SO_4^{2-} pair for instance, will be more likely to form CIPs than Mg^{2+}−Cl^- due to the high charged density sulfate ions. In the last four decades, due to its high charge density, Mg^{2+}−water systems with different anions have been frequently investigated to gain knowledge on CIP formation.[43, 45-57] In the $Mg(NO_3)_2$ aqueous system, at dilute to a fairly concentrated range (≤ 5.0 m), very little association occurs, and only with water-to-salt ratio WSR ≥ 6 (~ 9.0 m), various ion complexation occurs.[45, 54, 56, 58, 59] Complexes do not form in $MgCl_2$ solutions or $Mg(ClO_4)_2$ systems even at significantly high concentrations; complex formation certainly occurs in the $MgSO_4$ systems at medium to high concentrations.[60-64] Thus the solvated anion structure will have an impact on the hydration of the metal cations due to complex formation. Discussions on ion-specific effects have been extensively addressed by Collins and Kunz.[14, 65, 66] In the case of

weakened ion-dipole interactions such as found by replacing water with a smaller dielectric solvent like ethanol, ion association changes. For example, Mg^{2+}−Cl^{-} ion pair is more likely to form in ethanol than in water due to that Mg^{2+} is less electrically screened in ethanol.[67]

2.1.2 Ion Modes and Raman Spectroscopy

Raman spectroscopy is a useful tool to provide vibrational information of metal-water interactions. The microscopic ion-dipole, and even ion-ion electrostatic interactions in aqueous solutions can be captured spectroscopically in the low frequency region (200−400 cm^{-1}). Different vibrational frequencies and band shapes reflect different aqueous environments. The geometry of the first hydration shell of the hydrated magnesium cluster is considered to be octahedral, while for calcium the coordination geometry varies.[15, 42, 68-70] In an isolated octahedral system $M(H_2O)_6^{n+}$ of T_h symmetry, there are 51 normal modes of vibration and the irreducible representation is: $\Gamma_{vib}(Th) = 3a_g+a_u+3e_g+e_u+5f_g+8f_u$. These modes are made up of 18 internal and 18 external vibrations of the six-coordinated water molecules and 15 modes coming from the MgO_6 unit. The internal modes of the coordinated water molecules are OH bending and OH stretching at 1650 cm^{-1} and 3000 to 3500 cm^{-1}, while the external modes are weak librations in the 400-800 cm^{-1} region.[71] Rudolph et al. have extensively studied magnesium systems by assigning Raman and IR active modes for the MgO_6 skeleton, neglecting the internal vibrations of water associated with the structure of $Mg(H_2O)_6^{2+}$. [51, 63] Of the fifteen normal vibration modes associated with the MgO_6 skeleton, the Raman

active ones are $\nu_1(a_{1g})$, $\nu_2(e_g)$ and $\nu_5(f_{2g})$, where ν_1 and ν_2 are the Mg−O symmetric (ring breathing) and asymmetric stretch modes, respectively, and ν_5 the O−Mg−O deformation or ring deformation. In fact, the study of the magnesium-water interaction can be traced back as early as the 1950s.[72] The calcium-water stretch vibration, on the other hand, was not easily captured using Raman spectroscopy due to its weaker oscillation strength, yet Kanno and Rudolph et al. have report the detection of the mode.[44, 73]

Upon complex formation, the symmetry of the hydrate ions will change from O_h to lower symmetries depending on the degree of complexation. Spectroscopically, the lowering of symmetries will trigger more ion modes due to the degenerate modes such as "e" symmetry ones being split into modes of "a, b" symmetry. For instance, monodentate and bidentate have been observed experimentally upon complexation of acetate ion.[49] Moreover, complexation also is reflected on the anion modes. In $MgSO_4$ aqueous solution, a peak close to the sulfate symmetric stretch ν_1 (≈ 980 cm^{-1}) is considered a sign of CIPs, yet this assignment is rather controversial.[46, 61, 63, 74-76] Again, these CIP modes are rather weak, which also contributes to the debate. These modes however can be easily detected in the form of molten salts of $MgCl_2$, for example.[77, 78]

2.1.3 Water Modes in the Low Frequency Region and Hydrogen Bonding

The structure of water itself is fascinating. The tetrahedral structure of water is due to the four hydrogen bonds in its system, and because of this hydrogen-bonded tetrahedral structure, water exhibits unique properties such as high boiling point. In the

low frequency region of liquid water, the spectral features involve intermolecular interactions of water molecules. The various vibrations in this region can be described as librations or restricted rotations, hydrogen-bond stretchings or restricted translations.[79] Specifically in the terahertz region (0−300 cm^{-1}), two vibrations were detected at ~60 and 175 cm^{-1} and their assignments and nomenclatures vary. Different nomenclatures have often been given in the literature to these two bands such as H-bond bending and H-bond stretching, restricted rotation and restricted translation, perpendicular to O−H...O and parallel to O−H...O, transverse acoustic phonon and longitudinal acoustic phonon, standing wave (doubly degenerate) and standing wave (singly degenerate).[80] As Walrafen et al. showed the strong temperature dependence of these bands and confirmed the nature of the two bands, i.e. the intensity of hydrogen bonding stretch is severely weakened at high temperature due to the weakening of hydrogen bonded water structure.[80, 81] However, the frequency of this peak is not unambiguous since the same peak was detected at ~220 cm^{-1} at ambient temperature in a more recent Raman spectroscopic study.[82] This is partly due to the temperature and pressure applied to study the system and also different instruments. The center frequency change appears more significant when ionic salts are added. Upon addition of ionic salts, the hydrogen-bonded structure of water changes which appears in the spectral difference. Walrafen observed the most significant difference when halides were introduced to the system, while cations did not change appreciably the hydrogen bonding related vibrations.[79] Kanno et al revealed the difference brought by anions through the study of glass states of various magnesium salts. The frequencies for the hydrogen bond stretch were 190, 210, 200 cm^{-1} for chloride,

sulfate and perchlorate respectively; yet the frequency could be even higher because of the strong concentration dependency.[83] Other techniques evolved in the last decade. The main one is terahertz absorption spectroscopy. The stretching mode of hydrogen bonds in liquid water has been detected and theorized by Heyden et al. through terahertz (THz) spectroscopy and spatial decompositions of IR spectra.[84] The two contributing absorption modes of hydrogen bond stretching are at ~220 cm^{-1}, the third at 290 cm^{-1} is a silent band.[84] Traditionally, knowledge on structure changing effects can be gained from the study of the OH stretch region; now with the advent of terahertz spectroscopy it is possible to investigate the information-rich low frequency region, specifically the ion-water intermolecular interactions. Low frequency Raman spectroscopy is also information rich, and complementary to terahertz spectroscopy.

2.2 Raman Scattering Theory

When photons are scattered by an atom or a molecule, most of them experience Rayleigh scattering which returns the photons with the same frequency as the incident; only one out of 1000 goes through inelastic scattering and emits a photon of a different frequency.[85] This particular inelastic scattering phenomenon is known as Raman scattering. This weak intensity explains the very likely interference of observing Raman scattering from Rayleigh scattering. The frequency difference is called the Raman shift. Chemists are primarily interested in gaining molecular information such as vibrational frequencies of bonds in molecules and ions from the Raman scattering shift because molecules have vibrational modes each of which is at a particular frequency. The

scattered frequency is also unique for each mode. Two types of Raman scattering exist and are called Stokes and anti-Stokes scattering. The former occurs when the molecule is at its lowest energy state or ground state, and is excited to the virtual state which is much higher in energy than ground state, and then emitted back a photon with a lower energy state. The latter starts at an excited state, is then excited to a higher energy virtual state before returning to the ground state. The energy levels of the two Raman scattering along with Rayleigh scattering are illustrated in Figure 2.1. Stokes scattering is more common at room temperature since according to the Boltzmann distribution most molecules stays at the ground state. On a molecular level, Raman scattering occurs when there is a distortion of the electron cloud in a molecule due to the presence of an electric field. The ability to polarize the electron clouds is called polarizability. A Raman transition from one state to another is only allowed when the polarizability with respect to the normal coordinate is non zero, i.e. $\frac{\partial \alpha}{\partial Q} \neq 0$. Quantum mechanically, a Raman transition from an initial vibrational state *v* to a final vibrational state ν' associated with wave functions Ψ(ν) and Ψ(ν') may be allowed if and only if the transition moment integral $M_{\nu\nu'} = \int_{-\infty}^{\infty} \Psi^*(\nu')\, \hat{a}\, \Psi(\nu) d\tau$ where â is the polarizability tensor is nonzero. The Raman transition probability or strength is proportional to $M_{\nu\nu'}^2$ and to the squared electric field strength **E**. Therefore only certain vibrational modes in a molecule are Raman active, depending on the symmetry of the vibration mode; also the transition strength is unique to each mode.

2.3 Low Frequency Raman Spectroscopy

Raman spectroscopy utilizes excitation laser sources of known wavelengths, excites a sample to some virtual state and collects scattered light at a convenient angle to produce useful molecular information. The scattered intensity is proportional to the fourth power of the frequency (ω). Anti-Stokes shift is of higher frequency than the Stokes shift; however, due to the much lower population, at room temperature, Stokes shift is more commonly observed. The Raman shift generally can be expressed as the following:

$$\Delta\omega\ (\mathrm{cm}^{-1}) = \left(\frac{1}{\lambda_0\ (\mathrm{nm})} - \frac{1}{\lambda_1(\mathrm{nm})}\right) \times \frac{10^7 \mathrm{nm}}{\mathrm{cm}} \quad (1)$$

where $\Delta\omega$ is the Raman shift (Stokes or anti-Stokes) expressed in wavenumber (cm^{-1}), λ_0 is the excitation wavelength (nm), and λ_1 is the Raman spectrum wavelength (nm). In order to filter the strong Rayleigh scattering, a filter needs to be integrated into the detection system. For example, commercially available notch filters are built in a Raman probe. For example, a notch filter with a center frequency of 532 ± 2 nm, and a small blocking full width at half maximum (FWHM) of 13 nm will lead to a detectable spectral region of 490−520 nm (anti-Stokes) and 540−570 nm (Stokes). However in order to detect a Raman shift at 200 cm^{-1}, the Raman wavelength in Eqn. (11) needs to be less than 537.8 nm, which is out of the range of the above detectable region, not to say additional Rayleigh wing leakage may often occur.

A longpass filter may be employed to filter any light whose wavelength is shorter than a particular wavelength. For instance, a 535 nm longpass filter is thus capable of

filtering light of wavelength shorter than 535 nm and transmitting light of wavelength longer than 535 nm. Theoretically, with this filter, frequency region as low as ~100 cm^{-1} can be detected according Eqn. (1). However, a small amount of leakage may still occur due to the intense Rayleigh scattering and an insufficient optical density filter at the needed wavelengths.

2.4 Materials and Methods

2.4.1 Materials

Magnesium, calcium and sodium salts used in this work were: NaCl (Fisher Scientific, ACS certified, ≥99.0%), $NaNO_3$ (Fisher Scientific, ACS certified, 99.7%) , Na_2SO_4 (Fisher Scientific, ACS certified, 99.4%), $NaClO_4$ (Sigma Aldrich, ACS Reagent, ≥98%); $MgCl_2•6H_2O$ (Fisher Scientific, ACS certified, 100.0%), $Mg(NO_3)_2•6H_2O$ (Fisher Scientific, ACS certified, 98.9%), $MgSO_4$ (Fisher Scientific, ACS certified), $Mg(ClO_4)_2•6H_2O$ (Sigma Aldrich, 99%) ; $CaCl_2•2H_2O$ (Fisher Scientific, ACS certified, 100.0%), $Ca(NO_3)_2•4H_2O$ (Fisher Scientific, ACS certified, 101.0%) and $Ca(ClO_4)_2•4H_2O$ (Sigma Aldrich, 99%). Ethanol (Sigma Aldrich, 100%) was used to make equimolar mixtures with water. All aqueous solutions were made using ultrapure water with a resistivity of 18.1–18.3 MΩ·cm and a measured pH of 5.6 (the pH value is slightly acidic due to the dissolution of gaseous CO_2) obtained from a Barnstead Nanopure system (model D4741, Thermolyne Corporation) equipped with additional organic removing cartridges (D5026 Type I ORGANIC free Cartridge Kit; Pretreat Feed). Two concentrations 0.5 M and 2.0 M of each salt solution were studied in the low

frequency region by Raman spectroscopy, which corresponds to water-to-salt ratio of ~110 and ~28, respectively. Additional solutions of $MgCl_2$ and $CaCl_2$ of 4.8 and 6.4 M were made.

2.4.2 Methods. Low Frequency Raman Spectroscopy

A Raman setup that detects low frequencies was designed and utilized. The excitation source for the instrument was a diode-pumped Nd:YVO_4 laser (Millennium II, Spectra-Physics, San Jose, CA) which produces single-mode (TEM_{00}), *p*-polarized (>100:1 polarization ratio), 532.1 nm (second harmonic) continuous-wave light with an output energy of ~470 mW. It was then collected by a 5 mm focusing Raman probe (RPS532/12-10, Inphotonics, Norwood, MA) and focused on a sample contained in a glass vial. The light scattered at 90° to the excitation beam is focused onto the entrance slit of a monochromator (SpectraPro 500i, Princeton Instruments, Trenton, NJ) using a BK7 lens (7 cm focus length). The slit width was set to 100 μm. A 535 nm long-pass filter (Custom, Omega Optical, Brattleboro, VT) was placed in the light path before entering the monochromator equipped with a 1200 groove/mm grating and calibrated against the 435.833 nm emission line of a fluorescent Hg lamp. The scattered signals were detected with a liquid N_2-cooled deep-depletion CCD (1340/400 EB, Roper Scientific). These Raman spectra were acquired with 5 min of exposure time and averaged. The experiment was performed at ~22 °C. The experimental diagram is shown in Figure 2.2.

2.5 Results

2.5.1 Low Frequency Raman Spectra of Water

The Raman spectrum of water in a borosilicate glass vial was recorded and used as background (Figure 2.3). The main feature of water is a weak and broad band at ~230 cm^{-1}, which is assigned to the stretching mode of intermolecular hydrogen bonding as shown in Figure 2.4.[84] The band has been rarely described in any Raman studies.[82] However, this mode of water has been detected and theorized by Heyden et al. through THz spectroscopy and spatial decompositions of IR spectra.[84] The two contributing absorption modes of hydrogen bonds stretching are at ~220 and 290 cm^{-1}, although the latter is a silent band. The spectral region below 200 cm^{-1} and above 300 cm^{-1} of liquid water is associated with the restricted translational and librational modes of water, respectively.[71] In water-ethanol mixtures, the 230 cm^{-1} peak decreases in intensity as ethanol content increases and eventually disappears in pure ethanol. This is consistent with different hydrogen bonding strengths in water and in ethanol (Figure 2.3).

2.5.2 Low Frequency Raman Spectra of Magnesium- and Calcium-based Aqueous Salt Solutions

Metal-O_w Stretches (Ring Breathing Mode of MO_6)

The spectra of magnesium aqueous solutions provide the most interesting spectral features, while the spectra of sodium solutions, on the other hand, are rather featureless. The spectra of four magnesium salt solutions (perchlorate, chloride, nitrate, and sulfate) at concentrations of 0.5 and 2.0 M are shown in Figures 2.5 and 2.6 (raw and difference

spectra), along with that of neat water as reference. Compared to spectra of other salts, that of perchlorate exhibited a large background which may be due to fluorescence of perchlorate. A similar background was also found in calcium perchlorate and the study of Ruldoph et al.; yet no clear attribution was suggested.[73] At 0.5 M, the intermolecular Mg^{2+}–O_w stretch or more precisely MgO_6 ring breathing mode was very weakly observed at ~360 cm^{-1} for all salts. At 2.0 M, this peak was red-shifted by ~10 cm^{-1} for perchlorate, nitrate, and chloride salts. It was more significantly shifted for sulfate indicating a slightly different aqueous environment. Figure 2.7 illustrates this ring breathing mode of $M(H_2O)_6^{2+}$. The strength of this vibration is dependent on the cation; the counter anion also exerts a field that influences the vibration. In some cases such as sulfate, when the field is strong enough, a vibrational frequency shift is observable as it is in this study.

The spectra of three calcium salt solutions (perchlorate, chloride, and nitrate) at concentrations of 2.0 M were also obtained and are shown in Figure 2.8.(0.5 M spectra were shown in Appendix A).The Ca–O_w stretch however, was only clearly observed in $Ca(ClO_4)_2$ at 2.0 M at ~320 cm^{-1} particularly in the difference spectra. This band is significantly weaker and red-shifted by ~40 cm^{-1} compared to the Mg–O_w stretch but has a similar breadth.

Finally, the difference spectra of four sodium salt solutions (perchlorate, chloride, nitrate, sulfate) at concentrations of 0.5 and 2.0 M (sulfate being 0.25 and 1.0 M) were acquired. The 360 cm^{-1} mode was not observed in the low frequency region. The spectra are compared with those of magnesium salts in Appendix B.

Stretching Modes of Hydrogen-Bonded Intermolecular Water

Another major peak centered at ~230 cm^{-1} was observed in the spectra of both 2.0 M magnesium and calcium salt solutions, yet it was barely detectable in the sodium salt solutions. This peak shows a strong concentration dependency as it becomes more pronounced as concentration increases. At 0.5 M (or WSR ≈ 110), no ions perturbed the second hydration shell of "hydrated" water system (Figure 2.4 shows the first hydration shell of water), thus no enhancement of this band was found for the stretching mode of hydrogen-bonded intermolecular water. However at 2.0 M, significant enhancement was achieved due to increases Raman transition strength by addition charges from ions in the second hydration shell of water. If for example, one assumes that the second hydration shell consists of 18 water molecules, then at 2.0 M (or WSR = 27–28), some ions will be present in the second shell, which directly affects the polarizability of the tetrahedrally hydrogen-bonded water in the first hydration shell. Plots of the center frequency for the salt solutions are depicted in Figure 2.9. A "U-shaped" trend was revealed where the most weakly/strongly hydrated species have a higher center frequency than the intermediate ones. Perchlorate and sulfate were found to have much higher vibrational frequencies compared to chloride and nitrate which were fairly close to that of water.

2.6 Discussion

2.6.1 Metal–O_w Stretches

The slight spectral variation between different anions indicates a subtle difference in the coordination environment of Mg^{2+}. The octahedral geometry of the hexaaquo

$Mg(H_2O)_6^{2+}$ system has been thoroughly studied throughout the last century.[15-17, 71] Spectroscopic studies have shown that the Mg−O_w symmetric stretch usually lies in a fairly broad range centered around ~360 cm^{-1}, depending upon the counterion identity, concentration, temperature, and even pressure. In the present work, some spectral shifting was observed at two different concentrations. It is likely due to the alteration of the solvation environment for magnesium: at 0.5 M, more than 100 water molecules are available for every Mg^{2+} and its counterions, sufficient to constitute a full second hydration shell around magnesium; however, at 2.0 M only about 28 water molecules are available such that the second hydration shell for magnesium may not be complete. Hence, more Mg^{2+} will compete for oxygen sites of water, which restricts the vibration to a lower frequency. Sulfate behaved slightly different because of its high charge density that may possibly favors greater interactions with magnesium. According to the law of matching water affinities, strongly hydrated cations are more likely to interact with strongly hydrated anions.[14] In other words, it is more likely for species with equal water affinities to interact with each other. This is to say that Mg^{2+} and SO_4^{2-} are likely to electrostatically influence each other in a hydrated environment, which therefore leads to a slight frequency shift.

Several attempts have been made to identify the Ca−O mode, yet only in a recent paper by Rudolph et al. was it clearly captured and properly assigned.[73] This peak appears as a broad shoulder at ~290 cm^{-1}, i.e. at a peak position about 30 cm^{-1} away from the current study. The reason for this difference could possibly come from two factors: a difference in the salt concentration studied and the difficulty in determining the exact

position of this shoulder because of its weak intensity and large breadth. The difference between Ca−O and Mg−O stretches is due to the oscillation strength: the latter is considered much greater than the former because magnesium (II) binds water more strongly than calcium for it has a much larger charge density.[42]

2.6.2 Ion-Specific Effects on the Stretching Mode of Water

The enhancement of the 230 cm^{-1} band of ions on water became significant at 2.0 M where ions perturb the second hydration shell of water due to a change in polarizability of intermolecular water, which changes the Raman transition moment of this band. This effect was observed in both calcium- and magnesium-based aqueous salt solutions. The fact that the center frequency does vary slightly for different anions indicates that they interact with water differently, which agrees well with the difference in hydrogen bonding environments, *i.e.* $HOH\ldots OH_2$, $HOH\ldots OClO_3^-$, $HOH\ldots Cl^-$, $HOH...ONO_2^-$,and $HOH\ldots OSO_3^{2-}$. The U-shaped trend implies less restricted or stronger vibration strength for perchlorate and sulfate, two extremes of water structure-breaker and structure-maker, respectively. A similar ion trend was described by Kunz as it appears in some enzymatic activities.[65] Perchlorate is known to break the hydrogen-bonded structure of water. Therefore some water molecules will be loosely hydrogen-bonded to a large perchlorate ion, which gives a much "freer" vibration; sulfate on the other hand, because of its high charge density, increases the vibrational strength of tetrahedrally bonded water. Rudolph et al. assigned a similar broad band at ~242 cm^{-1} in $Mg(ClO_4)_2$ aqueous solutions to be associated with the $HOH\ldots OClO_3^-$ stretch which is very close to the position found in the

current work (~243 cm^{-1}).[51] However, the "linear" stretching vibration of $HOH\ldots OClO_3^-$ does not explain the vibrations in the neat water system as properly as the "breathing" motion of intermolecular water. Also, Cl^- and NO_3^- do in fact behaves like the boundary molecules according to the law of matching water affinity. Indeed, some computational modeling of intermolecular water and its salts solutions will provide more insight to the nature of these low frequencies vibrations.

Other Possible Assignments of the 230 cm^{-1} Peak

In the magnesium case, the peak might be associated with MgO_6 modes, specifically ν_5. This is supported by the study of Rudolph et al., as this band was observed in their Raman spectra and from computational results as shown in Table 2.1. Other results from the work of LaFont and Mink et al. are also shown in Table 2.1.[48, 72] The doubly degenerate ν_2 peak was too weak to be observed in aqueous solutions, yet it was detected in $MgSO_4 \bullet 7H_2O$ hydrates by Rudolph et al. [51]This experimentally determined ν_5 along with ν_2 is some 20 cm^{-1} different from computational results. In the calcium case, this band was not experimentally observed in the study of Rudolph et al. and the ν_5 falls below 100 cm^{-1} region from their computational calculation. Therefore this case is not very likely.[73]

Other possibilities regarding this band include: (1) a phonon resonance band from the fully hydrated Mg^{2+} system,[60] (2) $Mg^{2+}-Cl^-$ contact ion pairs (the lattice vibrational mode of A_g symmetry can be found at ca. 240 cm^{-1}) observed in molten salts and melts,[78, 86, 87] and (3) ion aggregation. All of these require a certain concentration limit or physical

condition, which clearly does not apply to our relatively low concentration range. Another possible assignment is the rattling motion of anions and cations as described by Funkner et al. in their THz spectroscopic study on monovalent and divalent halide salt solutions, yet these motions are usually found below 200 cm^{-1}.[88] More complex systems such as perchlorates have yet to be investigated.

2.7 Conclusions

Through this study, the Mg−O stretch was consistently observed in the ~350– 360 cm^{-1} region, which agrees well with previous studies. The Ca−O stretch was only clearly observed at ~320 cm^{-1} in $Ca(ClO_4)_2$ and deviates ~30 cm^{-1} from other studies of Rudolph et al. The unusually large discrepancy is due to the weakness of the mode itself; the strong background of perchlorate ions also makes it difficult to determine unequivocally the center frequency of the peak. The higher frequency and intensity of Mg–O stretch compared to Ca–O indicates a much stronger Mg^{2+}–water interaction. Water in the low frequency region has a significant vibration at ~230 cm^{-1} – the stretching mode of hydrogen-bonded intermolecular water. Anions play a major role by perturbing the hydrogen bonding network of water and change the frequency of this mode. Perchlorate and sulfate were found to perturb the water structure more significantly as indicated by the blue shift of the hydrogen bond stretch; this effect was not observed in chloride and nitrate systems. This agrees fairly well with the law of matching water affinities and shows that perchlorate and sulfate are indeed water structure-breaker (ions exhibiting weaker interactions with water than water itself) and structure-maker (ions exhibiting

strong interactions with water), respectively. Compared to anions, divalent cations studied here, Mg^{2+} and Ca^{2+}, were shown to have a much smaller effect on the hydrogen-bonded network of water, especially the vibrational frequencies of intermolecular water even though their interactions with water are fairly different.

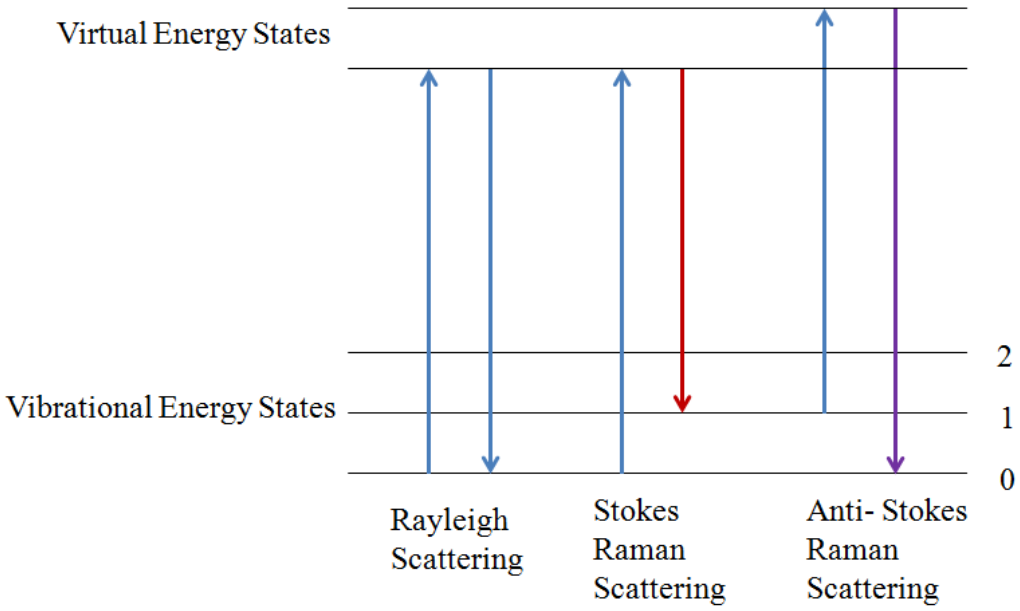

Figure 2.1 Energy-level diagram showing the states involved in Raman Scattering including both Stokes and anti-Stokes, along with Rayleigh scattering.

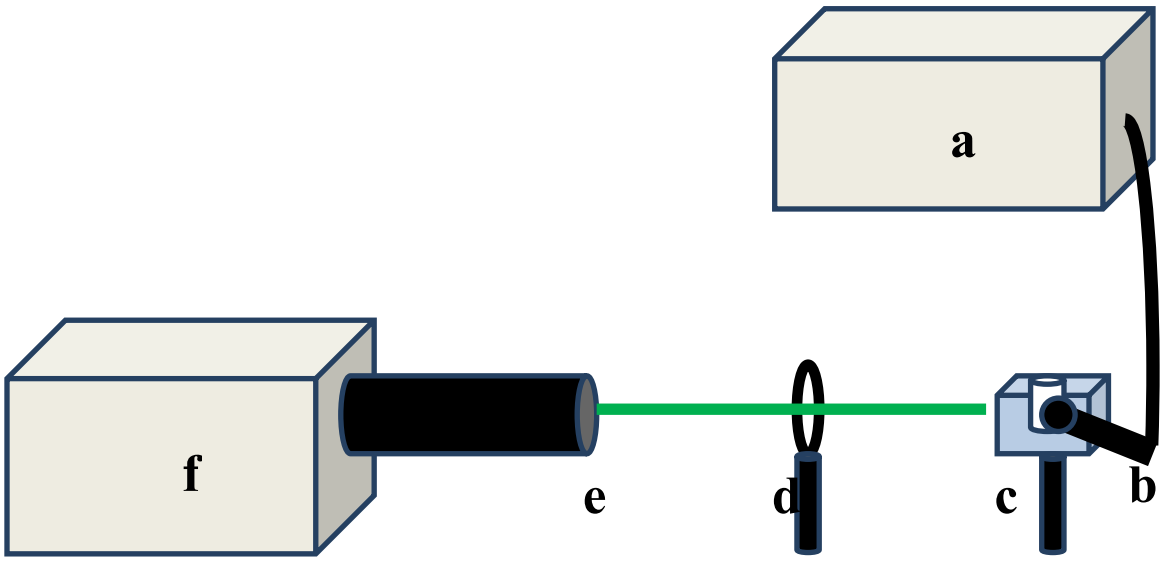

Figure 2.2 Schematic layout of the low-frequency Raman setup. (a) laser source, (b) fiber optic Raman probe, (c) sample holder, (d) focusing lens (FL = 75 mm), (e) 535 nm longpass filter, and (f) monochromator and CCD.

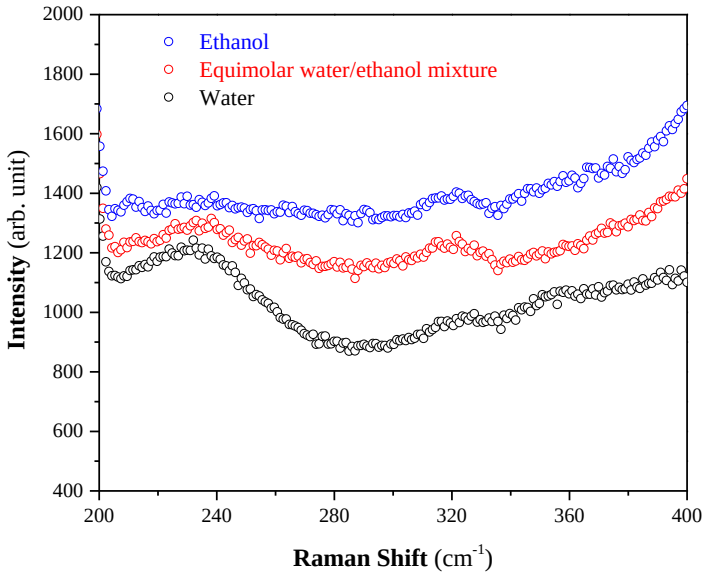

Figure 2.3 Raman spectra of water, ethanol and their equimolar mixture in the low frequency region.

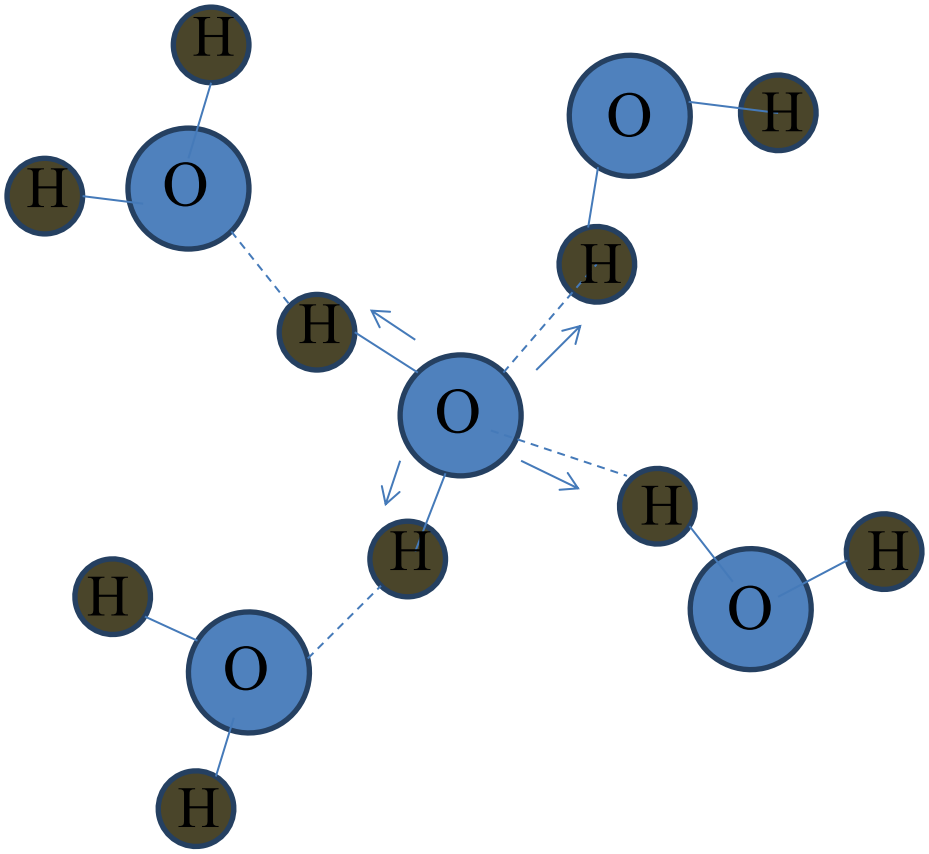

Figure 2.4 Stretching motion of hydrogen bonded intermolecular water.

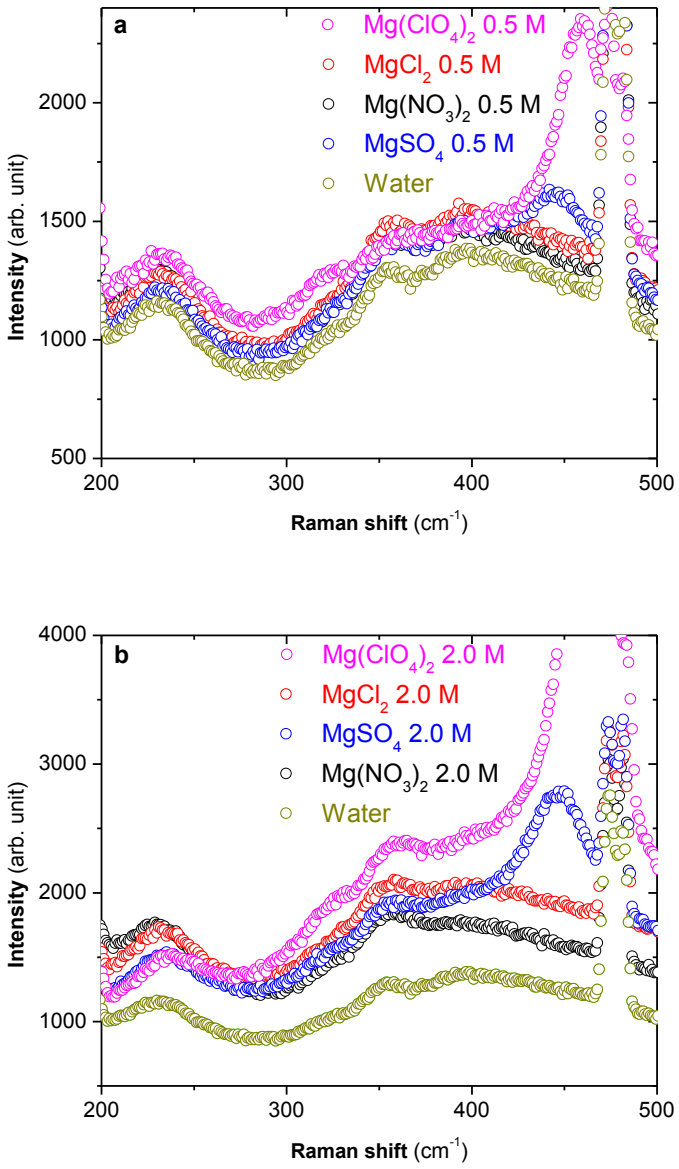

Figure 2.5 Raw Raman spectra of Mg salts in aqueous solutions at (a) 0.5 M and (b) 2.0 M.

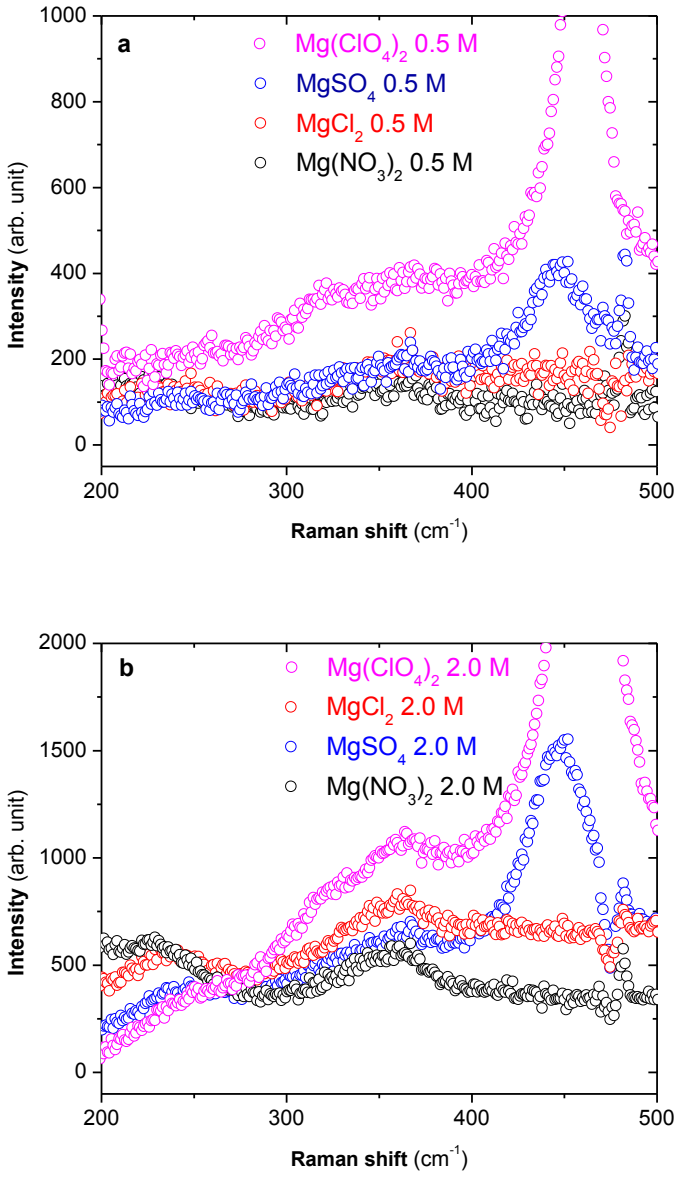

Figure 2.6 Difference Raman spectra of Mg salts solutions (a) 0.5 M and (b) 2.0 M. Water background was subtracted from the raw spectra.

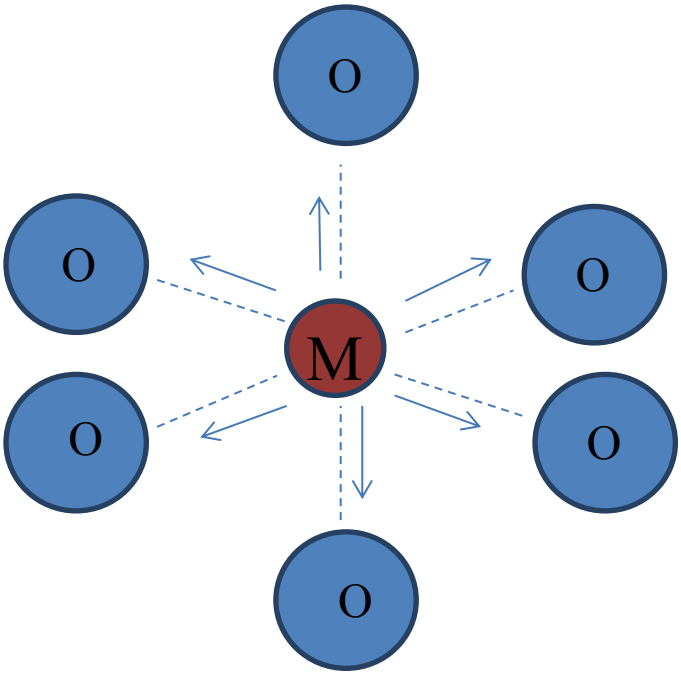

Figure 2.7 Ring breathing mode of MO_6 complex in the $M(H_2O)_6^{2+}$ octahedral structure.

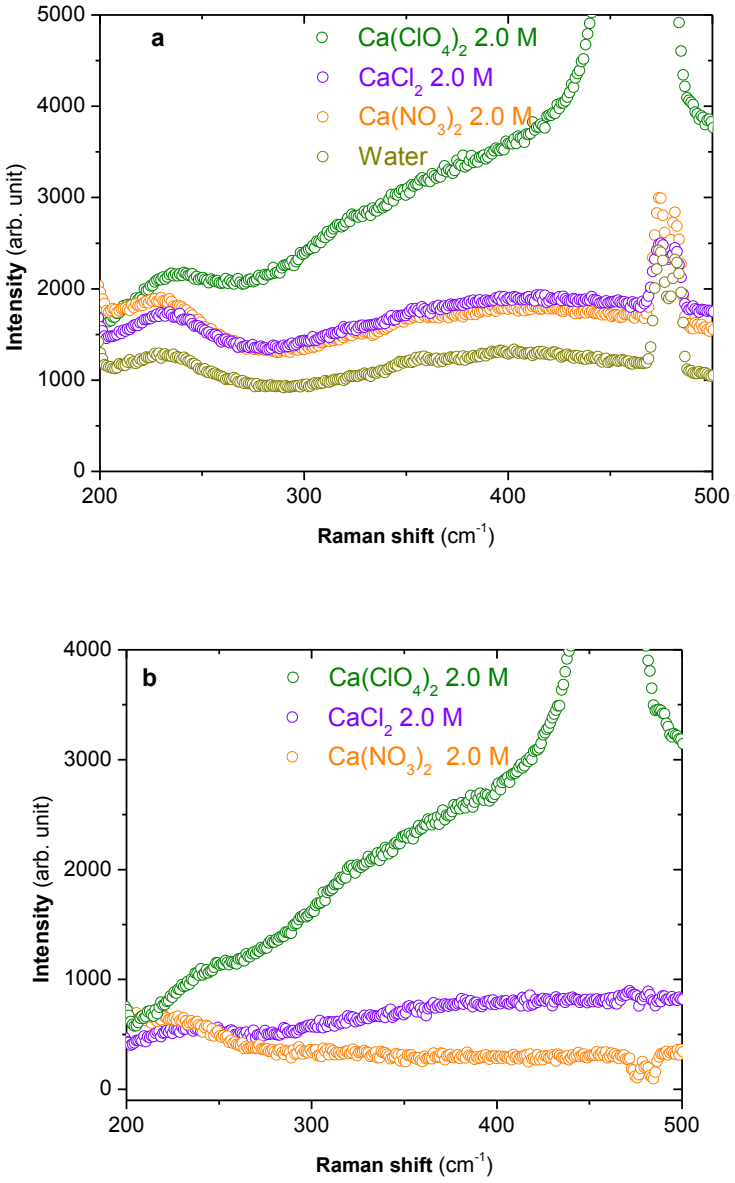

Figure 2.8 Raman spectra of aqueous calcium salt solutions. (a) Raw and (b) difference spectra. Water was used as reference.

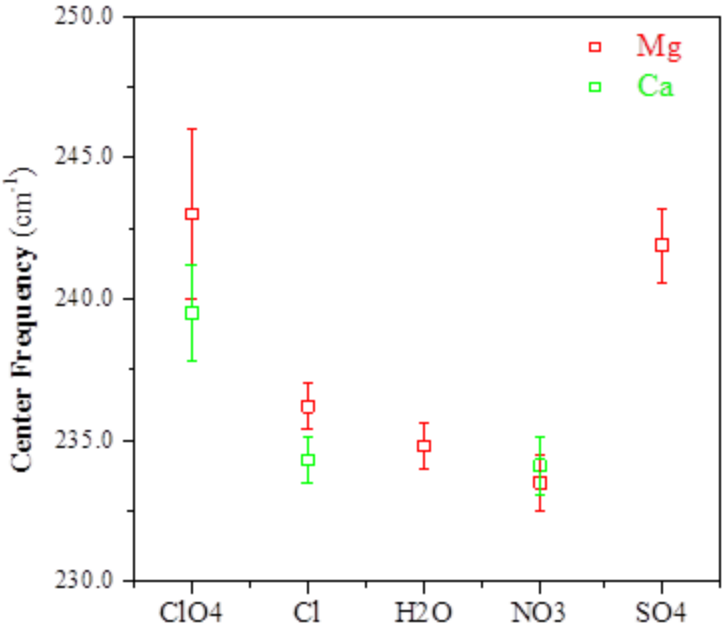

Figure 2.9 Center frequency variations of 230−240 cm^{-1} peak with different magnesium/calcium salt solutions at 2.0 M. The general trend is U-shaped: the most weakly/strongly hydrated species have a higher center frequency than the intermediate ones.

Table 2.1 Spectral assignment of MgO_6 modes from Raman spectroscopy and simulation results.

Raman mode	**Raman shift** [cm^{-1}]				
	Ref. 51		Ref. 48	Ref. 71	
	Exptl.[a]	Exptl.[b]	Exptl.[c]	Exptl.[d]	Calc.[e]
ν_1 (a_{1g})	370	370	365	357.5±0.5	356/(356)
ν_2 (e_g)	208	[205]	314	315±2	334/(286)
ν_5 (f_{2g})	258	258/251	216	240±4	264/(139)

[a] Frequencies were acquired from $MgSO_4 \bullet 7H_2O$. [b] Frequencies were acquired from $MgSO_{4(aq.)}$. Concentration was not specified. ν_5 at 251 cm^{-1} was obtained from calculations. [205] is an average of some measurements. [c] Frequencies were acquired from aqueous 3.0 M $Mg(ClO_4)_2$; [d] ν_1 and ν_5 were observed at a concentration of 2.213 mol/kg $Mg(ClO_4)_2$ at 23 °C, ν_2 is from the spectrum of $MgSO_4 \bullet 7H_2O$; [e] Unscaled HF/6-31G(d) frequencies of MgO_6 unit of the octadecaaqua magnesium(II) (T symmetry). Numbers in parentheses are scaled wavenumbers calculated by the same method of MgO_6 unit of the hexaaqua magnesium(II) (O_h symmetry).

Chapter 3

Ion-Silica Interactions in the Interfacial Region

3.1 The Silica−Water Interface

Silica has been receiving much attention from the scientific community because of its geochemical abundance and its wide application in nanotechnological devices. It has been utilized as optical fibers, packing materials in separation science, membrane devices in microelectronics, and as biosensing agent.[89-92] Among solid metal oxides, silica is the most abundant one in the Earth crust and the simplest case for experimental research and theoretical modeling on mineral oxide surfaces. Most studies on silica have been focused on its surface and interface or its modified and functionalized version with other species. Water−silica interactions, for example, have been extensively investigated with computational models such as molecular dynamics (MD) simulations and surface-specific techniques such as nonlinear optical spectroscopy. [93-99] The water−silica interactions are characterized by formation and dissolution which are two common geochemical processes. Three models are generally utilized to describe the dissolution process: electrical double layer, surface coordination, and crystal surface. The mineral/water interface is a charged surface, depending on the pH of the solution. The surface functional group of greatest abundance on hydrous mineral is the hydroxyl group

and adsorption occurs through coordinative interactions. The activities (diffusion and reaction kinetics) of different surface groups are controlled by surface sites, *i.e.* atoms at a step site is much more stable than atoms at a kink site.[100] The kinetics of the type of process were thoroughly studied by Rimstidt et al.[101, 102] They proposed the following geochemical reaction:[102]

$$SiO_2(s) + 2H_2O\,(l) = (SiO_2 \cdot 2H_2O)^* \quad (2)$$
$$(SiO_2 \cdot 2H_2O)^* \rightarrow H_4SiO_4(aq) \quad (3)$$

$$(SiO_2 \cdot 2H_2O)^* = SiO_2(s) + 2H_2O\,(l) \quad (4)$$
$$H_4SiO_4(aq) \rightarrow (SiO_2 \cdot 2H_2O)^* \quad (5)$$

Eqns. (2) and (3) describes the dissolution reaction and formation of silicic acid, whereas Eqns. (4) and (5) are the reverse processes of dissolution, precipitation. Also determined was the rate limiting step of the general reaction below is the breaking of siloxane bonds (Si−O−Si) due to the large activation energy (49.8 kJ/mol): [102]

$$SiO_2(s) + 2H_2O\,(l) \rightarrow H_4SiO_4(aq) \quad (6)$$

A detailed reaction mechanism of the breaking of siloxane and formation of silianol (Si-OH) groups was described by Michalske and Freiman.[103] The Michalske-Freiman model involves a water molecule process: (i) adsorption of water onto the Si−O−Si structure, (ii) electron and proton transfer to the Si−O−Si, the lone pair of electrons from the water's oxygen to Si, and proton from water to the bridging oxygen in Si−O−Si and

(iii) concerted processes involving the formation of Si−OH, SiO−H and breaking down of HO−H bond (an SN_2 process). [103-105] The process requires a solvent with a localized lone pair of electrons on one end and proton donor sites on the other hand.[103] However, mechanisms involving two water molecules have also been proposed.[106-110] For example, Cao et al. proposed that one water dissociates and forms two Si–O–H groups as described in the Michalske–Freiman model, while the other catalyzes the reaction.[106] In addition, Mahadevan et al. suggested two other pathways of silanol formation without breaking the siloxane bond.[96]

The rupture of the siloxane bond is a stress-induced corrosion by chemisorption (charge transfer) and physisorption (hydrogen bonding). The reaction shows strong temperature and pH dependencies. On the one hand, temperature impacts the diffusion rate of water molecules which exerts an influence on the reaction condition: reaction-limited vs. diffusion-limited.[101] For example, the logarithm of rate of dissolution reaction is found to proportional be to negative reciprocal of temperature. Hence at some temperature, rate limiting step of this reaction will be shifted from the rupture of the siloxane bond to the diffusion of silica away from the surface. On the other hand, pH changes the state of water and alters the reaction mechanisms. Below are the silica–water reactions occurring in the acidic and basic pH regimes:

$$> Si\text{–}OH + H_3O^+ \rightarrow > SiOH_2^+ + H_2O \quad (7)$$

$$> Si\text{–}OH + OH\text{–} \rightarrow > Si\text{–}O\text{–} + H2O \quad (8)$$

where >Si–OH represents surface silanol attached to the bulk SiO_2 structure. The pKa's of SiOH and $SiOH_2^+$ are 6.8 and 2.3, respectively, which indicates that at a pH below 2.3, the principal species are protonated, and above 6.8 are not protonated, and in between the majority is the neutral species.[111] Some studies show there are two kinds of surface silanol species which gives two pKa 's.[98, 112] When the overall surface charge density is zero, i.e. at the point of zero charge (pzc), the major species are unprotonated surface SiOH. The pzc of silica varies in the range 2−4 depending on the phase of the SiO_2 samples.[113] Nangia et al. found that the dissolution processes is much more facilitated by protonation and deprotonation of silica compared to neutral silanol species because the former are both two-step processes of two transition states and the latter involved one-step process with concerted bond-breaking and bond-forming processes in the transition state.[97]

The interactions between silica and water are mutual: water leads to the dissolution and precipitation of silica, whereas the state of silica surface groups influences the orientation of vicinal water molecules. According to a recent study by Sulpizi et al., two types of silanol groups are found at the surface of quartz: out-of-plane silanols with a strong acidic character (pKa = 5.6) and in-plane silanols with a pKa of 8.5. Water also exhibit two types: less coordinated and more coordinated water, shown by two broad bands located at ∼3400 and ∼3200 cm^{-1} representing the less ordered and more ordered tetrahedral structure of water.[98, 108, 114, 115] The behavior is interpreted as the outcome of surface silanol's ability to donate or accept hydrogen bonds with different strengths.[98] The signal 3200 cm^{-1} is enhanced at higher pH due to the enhancement of the

electric field at the surface by SiO^- which increases the number of more ordered or well-coordinated water molecules. One computational study shows that the surface silanol group influences water molecules at the first water layer which is within 3 Å of the oxygen atoms of the silica. Additional characteristic band at 1150 cm^{-1} assigned to HO(water)–H(SiOH) bending vibration can be detected via vibrational sum frequency generation (VSFG) spectroscopy.[94]

3.2 Impact of Ions on Water-Silica Interactions

Metal cation-silica interactions have been extensively investigated in the last decade by various methods in an effort to the understanding of promoted demineralization, ion-specific effects, and environmental purposes.[99, 116-119] The role of IA and IIA cations on modifying the interfacial water and silica structure is via adsorption process. Dove et al. proposed the following the equations to describe this interaction:[118]

$$> SiOH \; => SiO^- + H^+ \quad (9)$$

$$> SiOH + nH_2O \cdot M^{z+} => SiO^- - nH_2O \cdot M^{z+} + H^+ \quad (10)$$

$$> SiO - nH_2O + nH_2O \cdot M^{z+} => SiO^- - nH_2O \cdot M^{z+} + nH_2O \quad (11)$$

Where M^{z+} represents the metal cation with charge +z. Since all the species are in an aqueous environment, the nH_2O are used to represent the number of water molecules to

that are fully or partially hydrating the metal cation or surface silanol. When the cations is divalent, inner-sphere surface complexes may be also taken into consideration:

$$> SiOH + \mathrm{M}^{2+} + \mathrm{H_2O} => Si\mathrm{O}^{-} - \mathrm{M(OH)}^{+} + 2\mathrm{H}^{+} \quad (12)$$

However, outer-sphere complexes are still predominant in the interfacial region as suggested by many studies.[113, 120-122] The ability of promoting negative charge at the silica surface of IA and IIA cations follows the order of the "regular or direct" Hofmeister series for IA, in the order of $Li^+ < Na^+ < K^+$ and the reverse for IIA, $Ba^{2+} < Sr^{2+} < Ca^{2+} < Mg^{2+}$. Dove et al. argue that the order is due to the differences in the solvent structuring property of cations in the interfacial region and it is an entropically-driven process because the enthalpy of adsorption is comparatively smaller; they also came up with a specific parameter, the partial molal entropy, which corresponds well with their result.[123] In terms of interfacial water perturbation, Yang et al. describe the ability of monovalent cations in the order of $K^+ > Li^+ > Na^+$ by performing VSFG experiments; this order is a combining effect of size of hydrated cations and also the association strength.[119] The ion-specific effects can be summarized in Figure 3.1. Note that the net silica surface charge can create an electric field which again orients water molecules in a certain way.

While the role of metal cation at the aqueous silica interfacial region is relatively well known, oxyanion−silica interactions have yet to be recognized. Unlike hydrated cations, hydrated oxyanions generally interact with water less and thus creates more opportunities for adsorption processes to occur. By changing the surface charge of silica

to be slightly positive, anion−silica interactions can be favored over cation−silica ones, although even at neutral pH, some silanol groups are still deprotonated. Upon adsorption due to electrostatic forces or chemical bonding, as described in Section 1.2, the symmetries of the oxyanion are lowered, which can then be captured by surface-sensitive spectroscopic techniques. Recently Jubb et al. observe the adsorption process of sulfate ions onto hematite surfaces by the splitting of sulfate band at 980 cm^{-1} by total internal reflection (TIR)-Raman spectroscopy.[124] A similar pattern can thus be expected for other oxyanions−silica interactions using the same technique. In recent years, studies involving interactions between complex systems such ionic liquids and proteins have been researched due to the unique chemical properties silica exhibits and the application it extends to in these systems.[125, 126] The fundamental chemistry involving ion−silica interactions however is still not clear, and a better understanding needs to be provided.

3.3 Surface-Sensitive Techniques

Surface and interfacial properties of a material are significantly different from those of its bulk, even when the surface is in direct contact with ultrahigh vacuum (UHV).[127] Thus, there is a great interest in understanding this difference in order to gain control over important interfacial processes such as corrosion, passivation, materials processing (film growth and etching), and heterogeneous catalysis, which are frequently utilized in industrial manufacturing. For example, catalysis usually occurs at a metal surface through chemical bonding and electron transfer, the activation energy of certain reactions are thus lowered which significantly reduces the energy cost. Yet these

catalyzed reactions are only applicable at the metal surface, not to the bulk. Another example, surfactant molecules exhibit unique orientations at the interfacial region; they are surface-active such that their hydrophilic head are directly in contact with water, while their hydrophilic tails point to the air. A lot of membranes are based on this bilayer principle. This study involving ion interactions with water and silica head groups differ from bulk solvation or dissolution, since the event occurs only at the interfacial region. It is therefore necessary to utilize a surface-sensitive technique to probe it. Surface-sensitive spectroscopic techniques are generally achieved based on either of the two principles: (1) selection rules so that only molecules of a certain symmetry can be probed and (2) optical restriction so that light only travels to a confined distance within which molecules are probed.[128] Second order nonlinear techniques such as vibrational sum frequency generation (VSFG) and second harmonic generation spectroscopy fall in category (1). The penetration depths of these techniques are in the subnanometer region from the surface; the disadvantage is they are experimentally demanding, and results are difficult to interpret. On the other hand, TIR-Raman spectroscopy is based on the second approach where a "trapped" wave is utilized to probe molecules at the interfacial region. Also in category (2) is surface enhanced Raman scattering (SERS), where the electromagnetic field near the surface is amplified due to the excitation of localized surface plasmons and an enhance signal at the surface is generated. [129]

3.4 TIR-Raman Spectroscopy

Total internal reflection (TIR-) Raman spectroscopy is a common surface-sensitive technique to acquire molecular information at the surface or interface. This technique utilizes the fact that the excitation light is restricted to the interface when TIR occurs at or above the critical angle and detects the scattered light originated from the fast decaying evanescent wave propagating at the optically rarer medium side of the interface.

3.4.1 Snell's Laws of Reflection and Refraction

According to Maxwell's equations, three equations can be used to describe plane electromagnetic (EM) waves that travel at the interface of two isotropic and homogenous non-absorbing media:

$$\mathbf{E}_{\mathrm{i}}(\boldsymbol{u}, t) = E_{0\mathrm{i}} e^{i(2\pi n_i \boldsymbol{k_i}\,\mathbf{u} - \omega t)} \quad (13)$$

$$\mathbf{E}_{\mathrm{r}}(\boldsymbol{u}, t) = E_{0\mathrm{r}} e^{i(2\pi n_i \boldsymbol{k_r}\,\mathbf{u} - \omega t)} \quad (14)$$

$$\mathbf{E}_{\mathrm{t}}(\boldsymbol{u}, t) = E_{0\mathrm{t}} e^{i(2\pi n_t \boldsymbol{k_t}\,\mathbf{u} - \omega t)} \quad (15)$$

where **E** represents an electric field travelling in the direction **u**, a vector represent any three-dimensional space (*x*,*y*,*z*), with respect to time *t* and where the subscripts *i*, *r*, *t* denotes incident, reflected, and transmitted fields. n_{i} and n_{t} are the refractive indices of medium 1 and medium 2, where the incident and refracted beams, respectively. $\boldsymbol{k}$ represents the propagation or wave vector and ω is angular frequency of the wave. The

diagram is shown in Figure 3.2. Phase-matching conditions are applied at the interface (z = 0), such that:

$$n_i \boldsymbol{k_i u} = n_i \boldsymbol{k_r} \mathbf{u} = n_t \boldsymbol{k_t} \mathbf{u} \quad (16)$$

Arbitrarily the wave vectors can be chosen on the same plane, such that Eqn. (16) can be further reduced to give Snell's law of reflection and refraction:[130]

$$n_i \sin\theta_i = n_i \sin\theta_r = n_t \sin\theta_t \quad (17)$$

where θ_i, θ_r, and θ_t are the incident, refracted, and transmitted angles, respectively. The outcomes of Snell's relations are: (1) angle of reflection equals angle of incidence and (2) angle of incidence and reflection depends upon the refractive indices of the two media.

3.4.2 Fresnel Coefficients

The relations between the amplitudes of the reflected and transmitted waves to that of the incident wave at the interface are governed by the Fresnel coefficients:

$$r^p = \frac{E_r^p}{E_i^p} = \frac{\tan(\theta_i - \theta_t)}{\tan(\theta_i + \theta_t)}, \quad (18)$$

$$r^s = \frac{E_r^s}{E_i^s} = -\frac{\sin(\theta_i - \theta_t)}{\sin(\theta_i + \theta_t)}, \quad (19)$$

and

$$t^p = \frac{E_t^p}{E_i^p} = \frac{2\cos\theta_i \sin\theta_t}{\sin(\theta_i+\theta_t)\cos(\theta_i+\theta_t)}, \quad (20)$$

$$t^s = \frac{E_t^s}{E_i^s} = \frac{2\cos\theta_i \sin\theta_t}{\sin(\theta_i+\theta_t)}, \quad (21)$$

where r^p, r^s and t^p, t^s are the *p*- and *s*-polarized Fresnel reflection and transmission coefficients.

When the refractive index of medium 1 is greater than medium 2, i.e. $n_i > n_t$, there exists an angle at which all the light is reflected and none is transmitted. This angle is called critical angle (θ_c) above which TIR occurs. Mathematically it can be written as:

$$\theta_c = \sin^{-1}\left(\frac{n_t}{n_i}\right) \quad (22)$$

Above the critical angle the Fresnel transmission coefficients are imaginary:[128]

$$t_{Px} = \frac{2cos\theta_i(sin^2\theta_i - n_{ti}^2) + 2in_{ti}^2 cos^2\theta_i \sqrt{sin^2\theta_i - n_{ti}^2}}{n_{ti}^4 cos^2\theta_i + sin^2\theta_i - n_{ti}^2} \quad (23)$$

$$t_{Sy} = \frac{2cos^2\theta_i - 2icos\theta_i \sqrt{sin^2\theta_i - n_{ti}^2}}{1 - n_{ti}^2} \quad (24)$$

$$t_{Pz} = \frac{2n_{ti}^2 cos^2\theta_i sin\theta_i - 2isin\theta_i cos\theta_i \sqrt{sin^2\theta_i - n_{ti}^2}}{n_{ti}^4 cos^2\theta_i + sin^2\theta_i - n_{ti}^2} \quad (25)$$

where t_{Px}, t_{Py}, and t_{Pz} each represents transmission coefficient along each axis *x*, *y*, *z* for *p*- and *s*-polarized light. n_{ti} is denoted as the ratio of n_t and n_i for convenience.

3.4.3 Evanescent Wave and Penetration Depth

Under the TIR condition, there is not net transmission of energy across the interface between two non-absorbing media; however boundary condition still requires an electric field beyond this interface. This fast decay electric field is termed evanescent wave and it decays exponentially along the *z*-axis:

$$E = E_0 e^{-\beta z} \text{ where } \beta = \frac{2\pi}{\lambda}\left(\frac{sin^2\theta_i}{n_{ti}^2} - 1\right)^{1/2} \quad (26)$$

The penetration depth of this evanescent wave is the reciprocal of the exponential factor β in Eqn. (26):

$$d_p = \frac{\lambda}{2\pi}\left(\frac{sin^2\theta_i}{n_{ti}^2} - 1\right)^{-1/2} \quad (27)$$

where λ is the wavelength in vacuum and θ_i is the incident angle from the surface normal of the input beam. Since the intensity of the incoherent Raman scattering is proportional to the square of the magnitude of the electric field, the signal intensity decays twice as fast as the electric field:[128]

$$d_{RS} = \frac{\lambda}{4\pi}\left(\frac{sin^2\theta_i}{n_{ti}^2} - 1\right)^{-1/2} \quad (28)$$

where d_{RS} is the penetration depth of Raman scattering.

For most optical substrates used in TIR-Raman spectroscopy, this penetration depth usually lies in the range of 100−400 nm, i.e. about one magnitude smaller than that of similar techniques such as attenuated total reflection (ATR)-infrared spectroscopy.

3.5 Materials and Methods

3.5.1 Materials

Salts

Magnesium, calcium and sodium salts used in this work were: $NaNO_3$ (Fisher Scientific, ACS certified, 99.7%), Na_2SO_4 (Fisher Scientific, ACS certified, 99.4%), $NaClO_4$ (Sigma Aldrich, ACS Reagent, ≥98%; $Mg(NO_3)_2•6H_2O$ (Fisher Scientific, ACS certified, 98.9%), $MgSO_4$ (Fisher Scientific, ACS certified), $Mg(ClO_4)_2•6H_2O$ (Sigma Aldrich, 99%); $Ca(NO_3)_2•4H_2O$ (Fisher Scientific, ACS certified, 101.0%), and $Ca(ClO_4)_2•4H_2O$ (Sigma Aldrich, 99%). NaCl (Fisher Scientific, ACS certified, ≥99.0%) was used as background electrolyte salts.

Aqueous Solutions

Two concentrations (0.25 and 0.5 M) of these aqueous solutions were made using ultrapure water (18.1–18.3 MΩ·cm, NanoPure, Barnstead/Thermolyne). 1.0 M and 1.5 M NaCl solutions were made as two background electrolyte solutions. Solution pH was controlled by adding concentrated HCl (37% wt., Fisher, trace metal grade, Fisher

Scientific) dropwise until pH ~2.0 was reached. The added volume of HCl was small enough not to significantly alter the solution concentration. The pH of solutions was measured with a standard pH meter (Ag/AgCl glass electrode, Accumet AB15, Fisher Scientific) which had been calibrated properly.[131]

3.5.2 Methods

TIR-Raman Measurements at the Silica/Aqueous Solution Interface

The TIR-Raman spectrometer setup used in this study is described elsewhere by Jubb et al.[124] A similar diagram is shown in Figure 3.3. This instrument utilized a diode-pumped Nd:YVO_4 laser (Millennium II, Spectra-Physics) as an excitation source which produces single-mode (TEM_{00}), *p*-polarized (>100:1 polarization ratio), 532 nm (second harmonic) continuous-wave light with output energies of up to 1 W. An output energy of 690 mW laser beam was applied in all silica/solution systems to optimize acquisition time and avoid damages on the fused silica hemispherical prism. The beam was guided to the sample flow cell by a set of four silver mirrors and then focused onto the silica/solution interface via a 5 cm focal lens. In order to control the incident angle to the desired direction, a manually controllable goniometer arm was installed. The last mirror and a focal lens, along with two irises were mounted on the goniometer arm. All spectra were collected with an incident beam angle of 73° from the surface normal, therefore above the critical angle of the silica/solution ($\theta_c \approx 66.3°$) interface. The Raman scattered light from the interface was collected by a 50× objective lens (Nikon) and refocused into

a 535 nm longpass filter (Omega Optical, Custom) before entering a monochromator (SpectraPro500i, Princeton Instruments).

The TIR-Raman experiments were carried out using a bare fused silica hemisphere (25.4 mm diameter × 12.7 mm height, surface quality 60/40, ISP Optics Inc.). All fused silica hemispheres were cleaned before use by rinsing with large amounts of nanopure water. All silica/solution TIR-Raman spectra were an average of five spectra with 2 min acquisition per spectrum. The last set of experiments with increased ionic strength (without NaCl, with 1.0 M and 1.5 M NaCl) were measured at 1 min acquisition time because of improved S/N ratio. The spectra of silica/water were checked at the beginning and end of each day that experiments were run to ensure system stability, reproducibility, and reversibility of ion adsorption. In a typical TIR-Raman experiment the solution was prepared, conditioned, and then pumped in to the flow cell by a peristaltic pump (MasterFlex L/S, Cole-Parmer) and out to a waste disposal jar. Between two consecutive trials, ultrapure water was used to clean the silica surface to make sure no ion adsorbs onto the surface.

Bulk Raman Measurements of Aqueous Solutions

The same excitation source was used as in the TIR-Raman measurements and then collected by a 5 mm focusing Raman probe (RPS532/12-10, Inphotonics, Norwood, MA). The beam was applied at the sample with an output power of 470 mW and the backscattered light entered the monochromator (Andor Shamrock, SR303I-A) equipped

with a CCD camera (Andor Newton) manually calibrated with naphthalene standard peaks.

Refractive Indices Measurements

In order to determine the penetration depth of different silica/solution systems, a Zeiss refractometer (Model 51968, Carl Zeiss, Germany) was used. Sample solutions were illuminated by white light and measurements were performed at ambient temperature.

3.6 Results

3.6.1 Penetration Depth

The measured refractive indices of the aqueous solutions are found in Table 3.1. According to the user's manual of Abbe Zeiss Refractomer, a white light is commonly used to illuminate the sample, and this so obtained exactly corresponds to that of sodium D-line (wavelength = 589 nm).[132] The obtained refractive indices compared to that by 532 nm wavelength light are fairly close. The refractive index of water at 532 nm is approximately 1.3365 at ambient temperature and pressure, that at 594 nm, close enough to 589 nm, is 1.3345.[133] Therefore, the difference of refractive indices between 532 nm vs. 589nm is less than 0.002. Although the wavelength dependence of other salt solutions may vary, we estimate this difference will be more or less in the same order of 0.002. A plot of the penetration depth vs. refractive index of the aqueous solution for the silica/aqueous solution interface is shown in Figure 3.4, where the refractive index of

fused silica is 1.46071.[134] As the refractive indices of aqueous solutions vary from 1.3320 to 1.3445, the penetration depth lies in the range of 134−150 nm, which corresponds to a couple of hundred water layers. The difference of penetration depth by 532 nm and 589 nm will be a couple of nanometers in this range. However, the evanescent wave decays exponentially, therefore the signal from the first ten water layers (including the interface) contributes more than the next tenth. As the wave propagates deeper in the bulk, its electric field gets much weaker therefore the scattered light becomes fairly insignificant. Another reason for the surface sensitivity of the technique is that most of the scatterers probed come from the Debye layer, the most "concentrated" layer where electrostatic interaction, chemical reaction, and adsorption occur. Yet we admit some bulk signals were also acquired.

3.6.2 Bulk Raman Spectra of Aqueous Solutions

The bulk Raman spectra of magnesium calcium and sodium oxyanions perchlorate, nitrate and sulfate salt solutions at 0.25 and 0.5 M at pH 2 are shown in Figure 3.5. The symmetric stretch ν_1's for hydrated ClO_4^- , NO_3^- and SO_4^{2-} are detected at ~930, ~1040 and ~980 cm^{-1}, NO_3^- and SO_4^{2-} peaks are fairly symmetric; the asymmetry in ClO_4^- are due to a shoulder which is assigned to be second overtone of ClO_4^- bending by Lutz and others.[135-137] Note that as the concentration goes from 0.25 to 0.5 M, the peaks get more intense and slightly broadened. Other than the symmetric stretch ν_1 mode, bending and asymmetric stretches are also visible in the spectra. Sulfate differed from other oxyanions by the appearance of a tiny peak at ~1050 cm^{-1} which is assigned to bisulfate symmetric

stretch v_1 mode.[62] This indicates protonation occurs in sulfate but not nitrate and perchlorate aqueous solutions. The bulk study confirms a higher acidity constant for nitric and perchloric acid compared to bisulfate.

3.6.3 TIR-Raman Spectra of the Silica/Aqueous Solutions Interface

At 0.25 M, TIR-Raman spectra resemble bulk spectra shown in Figure 3.6a−c. TIR peaks of oxyanion modes were generally broader compared to sharp peaks in bulk which signified the inhomogeneous environment the oxyanions situated in. (**However, caution needs to be taken when the center frequency of these oxyanion modes are compared between the bulk and TIR measurements; more careful calibration will be performed to further evaluate these frequencies.**) One significant difference appears in perchlorate spectra, which shows the emergence of the $HClO_4$ v_1 stretch, a weak medium width peak at 1012 cm^{-1}, close to the assignment given by Ratcliffe and Irish in their bulk study. TIR-Raman spectra of NO_3^- show no observable change from the bulk, whereas SO_4^{2-} remains somewhat protonated as the appearance of HSO_4^- mode is still detectable at the surface. At 0.5 M, these phenomena are more pronounced as shown in Figure 3.7a-c. The v_1 modes of $HClO_4$ and HSO_4^- get more intense; that of HNO_3 emerges as a broad shoulder from the asymmetric peak of nitrate mode, centered around 1300 cm^{-1}, similar to that observed in bulk solution. This shoulder is clearly not in the bulk spectra of any nitrate salt solutions, therefore proving the surface sensitivity of the technique.

3.6.4 Surface Acidity

The evolution of protonated species follows the order HSO_4^- < $HClO_4$ < HNO_3. Acid dissociation constants can be extracted using the following formula:

$$[HA] \leftrightarrow [H^+] + [A^-] \quad (29)$$

$$pH = pKa + \log([A^-]/[HA]) \quad (30)$$

since

$$[A^-]/[HA] = \text{Area } (A^- \nu 1 \text{ stretch}) / \text{Area } (HA \nu 1 \text{ stretch}) \quad (31)$$

where $[A^-]$ and [HA] are acid and base conjugate pair. Eqn. (30) is called the Henderson-Hasselbach equation. A number of assumptions were at the interface when using Henderson-Hasselbach equation to determine acid dissociation constants: (i) pH ≈ 2, (ii) no CIP formation, (iii) $[H^+]$ is delocalized, and (iv) $[H_2SO_4] \approx 0$. (i) and (iii) assume the proton concentration at the interface to be close to that of the bulk and there is no localized pH at the interface. These two assumptions are still under debate, yet the interfacial pH can be certainly be different from the bulk.[138] The magnitude of the difference is not certain. Different analyte solutions can affect this interfacial pH differently.[139] In fact, the delocalization of protons may not be valid since different surface silanol groups with different pKa's are present in the interfacial region as discussed in earlier sections. Hence this primitive model needs to be improved in the future. (ii) is reasonable since CIP formation requires high concentration of both anions

and cations at the interfacial region; yet at low bulk concentrations such as 0.5 M, we infer the interfacial concentration will certainly be less than 3.0 M. In addition, hydrated metal cations forming outer sphere complex with the surface silica is more energetically favored.[118] (iv) takes Le Chatelier's Principle into consideration that the second degree of protonation is hindered for the second proton may not be easily stabilized. Also, no spectral evidence suggest the emergence of any mode from H_2SO_4, although a spectral limitation of detecting H_2SO_4 modes occurs, that is the significant overlap of modes from the acid and its two conjugated bases which appears in bulk studies.[140] Once spectra were fitted, the calculated pKa were: $HClO_4$ (0.4) < HNO_3 (0.7) < HSO_4^- (0.8) (Figure 3.8). The acidity constants at the interface for the three acids are not significantly different from each other. On the other hand, if a constant pKa in the bulk and in the interfacial region is assumed, the interfacial pH can be determined, similarly, although pKa values are generally different in different salvation environments. The interfacial pHs of three different oxyanion solutions are: NO_3^- (-0.2 ± 0.1) ≈ ClO_4^- (0.0 ± 0.3) < SO_4^{2-} (3.2 ± 0.6) (Figure 3.9). This results show the different surface modifying abilities of the three oxyanions: nitrate and perchlorate tend to give a positively charged surface, and sulfate tends to generate a more neutral surface.

3.6.5 Charge Screening Effect

When 1.0 M NaCl background salt was added to the 0.25 M aqueous salt solutions, the intensity of the protonated peaks of oxyanion symmetric stretch ν_1 increased noticeably as shown in Figure 3.10a-c. A quantitative analysis of peak areas shown in

Figure 3.11 of the ν_1 mode shows a consistently larger peak area in the spectrum with NaCl compared to that without NaCl. Three possible explanations for this phenomenon are: (1) increased Raman transition strength (2) charge screening and (3) double layer effect. (1) The addition of background electrolytes into the system introduced charges around these vibrations from oxyanions, which increases Raman transition strength of these modes. The phenomenon is explained in the previous chapter. (2) Charge screening shifts the equilibrium of reaction (32) towards the unprotonated oxyanion site. Once unassociated ion pairs (Si-OH_2^+ and A^-) forms, these charged are immediately screened by hydrated background electrolyte (Na^+ and Cl^-), shifting the chemical equilibrium toward the reverse direction. Solubility of many ionic salts increases upon addition of electrolyte salts based on the same reason.

$$\mathrm{Si-OH_2^+ + A^- \leftrightarrow Si-OH + HA} \quad (32)$$

(3) The electrical double layer (EDL) governs the charge at the surface is screened by ions in the interfacial region. The Debye length is a measure of the thickness of the double layer. It was shortened as ionic strength of the solutions increased upon addition of NaCl salts, hence more oxyanions were squeezed to the charged surface and screening the surface, which gives an enhancement of the scattering signals, compared to the without NaCl case. **A bulk study of ionic strength effects on these oxyanion modes to differentiate whether the enhancement comes from (1) and (2) versus (3) will be conducted in future experiments.**

3.7 Discussion

3.7.1 Protonation in the Interfacial Region

A few representative ligand free energy relationships (LFER) to describe inner- and outer-sphere complexes are summarized by Stumm.[100] A number of possibilities regarding bulk interaction and surface complexation are: (1) metal complexation with solute molecules vs. formation of surface complex, (2) metal ion hydrolysis vs. surface complex with oxygen donor atoms, and (3) ligand protonation vs. binding to the surface central atom.[141-143] Some difficulties in examining metal cation−silica surface interactions are posed due to a huge background from the silica substrate which prevents any detection below 900 cm^{-1}. As discussed in detail in Chapter 2, the metal-water interactions are in the region below 900 cm^{-1}, thus direct detection of metal-water interactions at the surface through this setup is impossible. Case (3) may be a more appropriate description of the oxyanion−silica surface interactions. Two competitive processes occurring at the interface are:

$$A^{z-} + H^{+} \leftrightarrow HA^{1-z} \qquad (33)$$

$$A^{z-} + > MOH_2^{+} \leftrightarrow > MA^{1-z} + H_2O \qquad (34)$$

Eqn. (34) is less likely to take place since silica is not a good electron pair acceptor to form surface complexes. Therefore, it is believed the surface adsorption occurring in the present study is proton transferring process. Dzomzak and Morel found the pK_2 for SO_4^{2-} (or, pK_a for HSO_4^{-}) in hydrous ferric oxide to be ~2, which doubles the value from this

study. This is understandable because the surface reactions will be mineral-specific; different surface groups have different affinities for protons and their ability to alter the interfacial aqueous environment will be different.

In utilizing the Henderson-Hasselbach, whether assuming an invariant pKa or pH in the interfacial region, SO_4^- deviates from the other two oxyanions in terms its ability to modify the charged surface or be modified by the charged surface. Although it being diprotic acid may partially explain this, the ion specific effects predominately determines its interaction with water and other charged surfaces.

3.7.2 Penetration Depth and Enhancement of Oxyanion Mode

A further study of ionic strength effect on oxyanion mode was conducted by increasing the NaCl from 0, 1.0 to 1.5 M. The result was rather consistent: the intensity of oxyanion peak increases in the order of 0, 1.0 to 1.5 M for all the salts tested. Spectra were shown in Appendix C. As mentioned in early sections, three possible reasons are increased Raman transition strength, charge screening shifted equilibrium and EDL effect. The first two are not convoluted in the present study since once charges are introduced into the system, both effects simultaneously take place. A computation model can certainly provide some insight through controlling one and varying the other. In fact, the story is more complex because it is at the surface. The EDL effect is surface/interface-specific. As stated in the earlier sections, more scatterers are squeezed

to the surface region upon addition of NaCl. The Debye length can be calculated via the following equation: [144]

$$\lambda_D = \left(\frac{\varepsilon_0 \varepsilon_r k_B T}{\sum_{j=1}^{N} n_j^0 z_j^2 e^2}\right)^{1/2} \quad (35)$$

where ε_0 is the electric constant, ε_r is the relative static permittivity, k_B is the Boltzmann constant, T is temperature, n_j is the bulk concentration of the j^{th} species in the solution, z is the charge of the j^{th} species, e is the elementary charge. The Debye length of $Mg(NO_3)_2$ at 0.25 M for example, changes from 0.2 nm to 0.11 nm upon addition of 1 M NaCl background salt, which is about 50% of difference. More information on Debye length vs. ionic strength is given in Table 3.2. As the electric field is strongest at the surface, this will enhance the oxyanion mode to some degree. Some may argue that the enhancement of oxyanion peak area is from the increased penetration depth as the ionic strength of the solutions increased. The difference of refractive indices in the with and without case is around 0.01 which gives about 10-15 nm. This difference is believed to contribute insignificantly to the Raman scattering intensity, which is shown to the integrated evanescent wave intensity along z direction: [145]

$$I_{I+B} = I_0 \int_0^{\infty} C_{I+B}(z) e^{-z/d_p} dz \quad (36)$$

where I_{I+B} is the Raman intensity contribution from the interfacial region and the bulk, I_0 is the intensity of the incident beam, C_{I+B} is the property of the solution: it is proportional to frequency to the fourth, scattering cross section, and scatter density. It is clear that the

concentration of ions at a charged surface decays following a Poisson-Boltzmann distribution in the diffuse layer,[146] and the evanescent wave also decays exponentially, therefore scattering contributed from 150 – 160 nm region is close to zero. Again, a computational profile of this integrated Raman intensity will still be beneficial to our understanding.

3.8 Conclusions

Adsorption at charged aqueous silica interface is characterized by the protonation process of oxyanions. Protons were shown to be transferred from silica surface sites to interfacial oxyanions, which led to the appearance of acid symmetric stretching mode detected by TIR-Raman spectroscopy. The interfacial pHs of several oxyanion solutions were extracted from spectral information using a primitive Henderson-Hasselbach relation: NO_3^- (-0.2 ± 0.1) ≈ ClO_4^- (0.0 ± 0.3) < SO_4^{2-} (3.2 ± 0.6), which differs significantly from the bulk (2.0 ± 0.2). Therefore, a different silica-water interface is suggested: in nitrate or perchlorate solutions, the surface are more positively charged while in sulfate solutions, the surfaces are neutrally charged. The effect of background electrolytes on the protonation process was further investigated. With the addition of 1.0 M NaCl solutions, non-protonated oxyanions symmetric mode was largely enhanced due to the fact that the compressed electrical double layer gave rises to more scatterers being probed. The more compact double layer therefore severely hindered the protonation process of oxyanion in the interfacial region. A computational model however, is still needed to provide better understanding on the structure and composition at the charged

silica/water interface and the changes brought by background electrolytes. Furthermore, the effect of cations on modifying the interfacial region is worth exploring in the future.

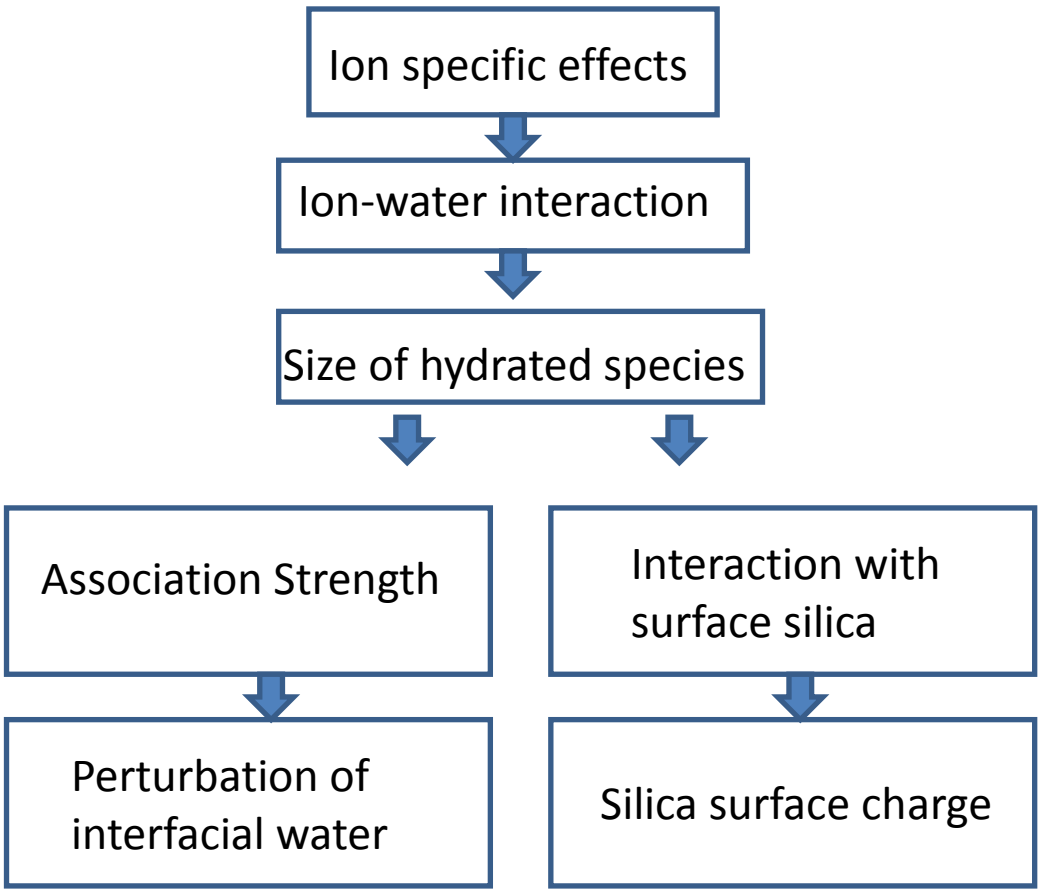

Figure 3.1 Diagram of the impact of ions in the silica/water interfacial region.

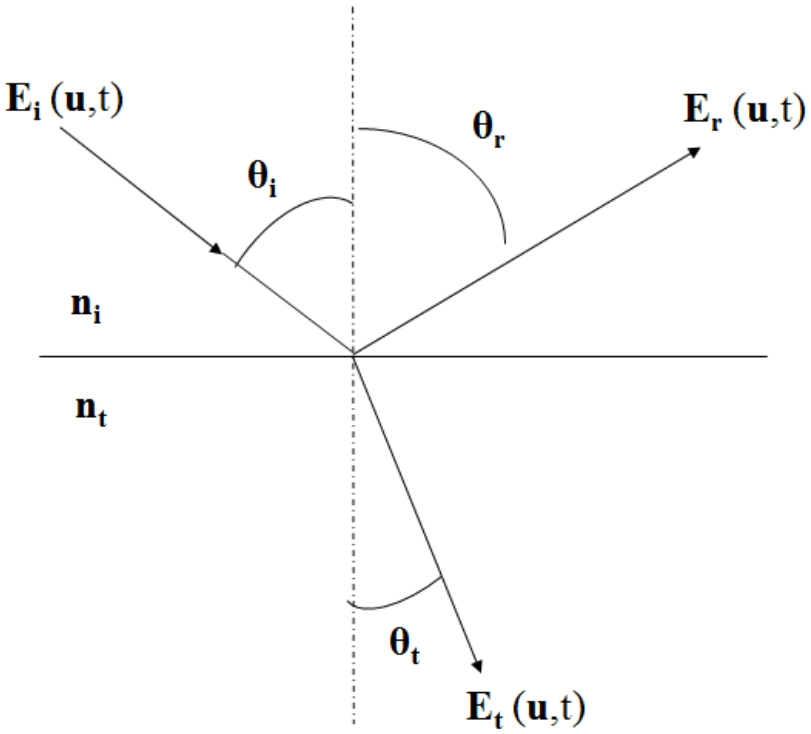

Figure 3.2 Diagram showing electromagnetic waves propagating at the interface.

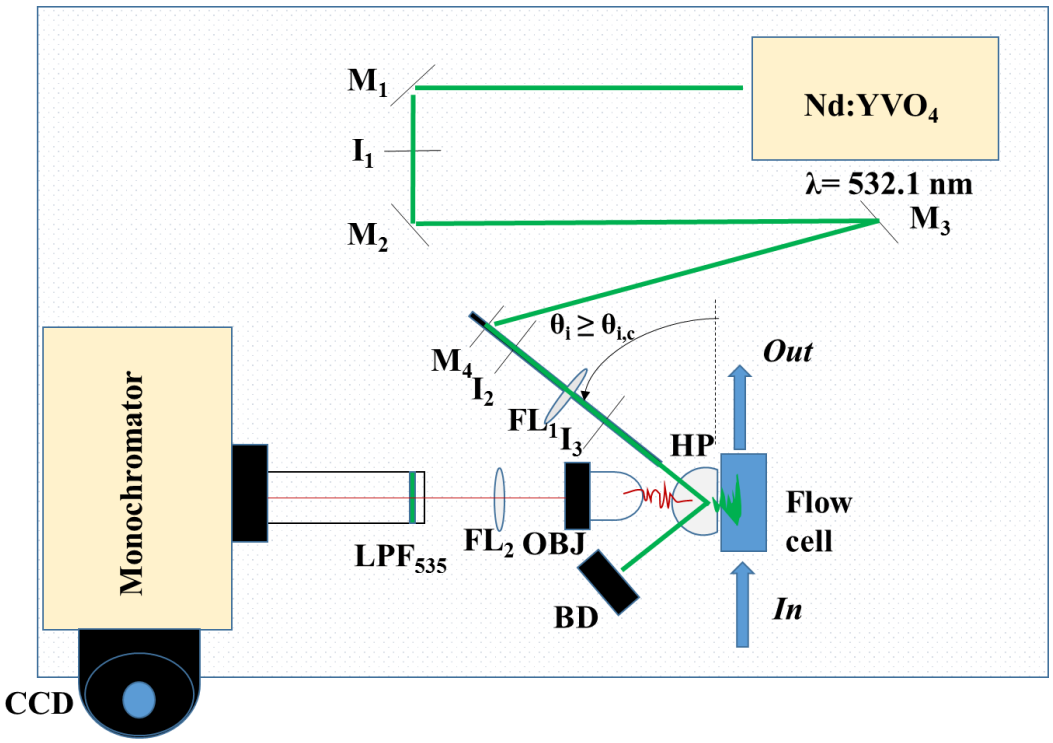

Figure 3.3 Schematic representation of the TIR-Raman setup. The input beam goes through several optical components including Ag mirrors (M), irises (I), focusing lenses (FL) before arriving at the planar face of a hemispherical prism (HP). The reflected input beam is directed into a beam dump (BD). The Raman scattered beam generated at the prism/solution interface is collected by a microscope objective (OBJ) and filtered by a 535 nm longpass filter (LPF) before entering the monochromator and the charge-coupled device (CCD) camera.

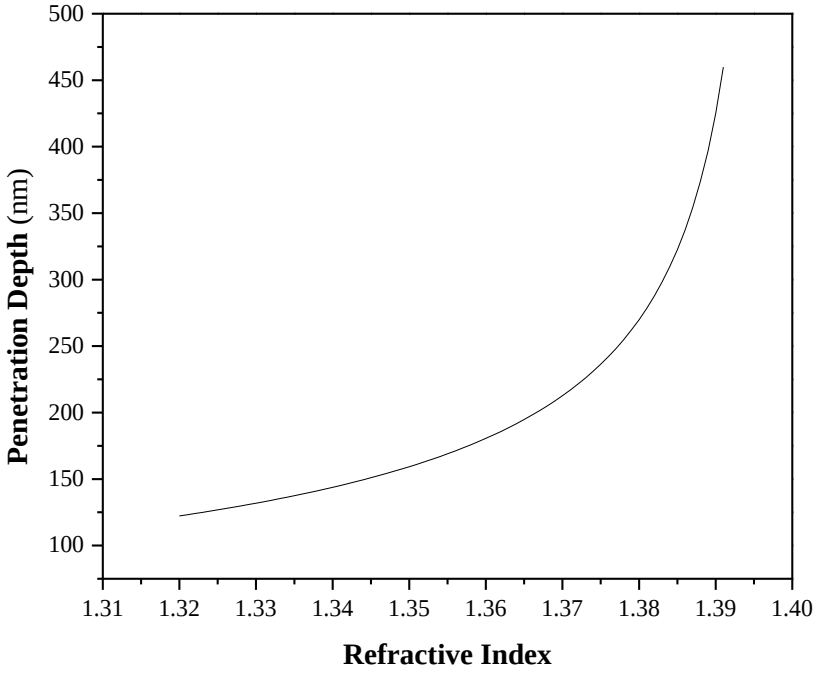

Figure 3.4 Simulation penetration depth at the silica/aqueous salt solutions interface as a function of refractive indices of solutions. Eqn. (28) was used where the incident angle is $\theta = 73^{\circ}$, excitation wavelength λ = 532 nm, refractive index of fused silica n_i = 1.46071.

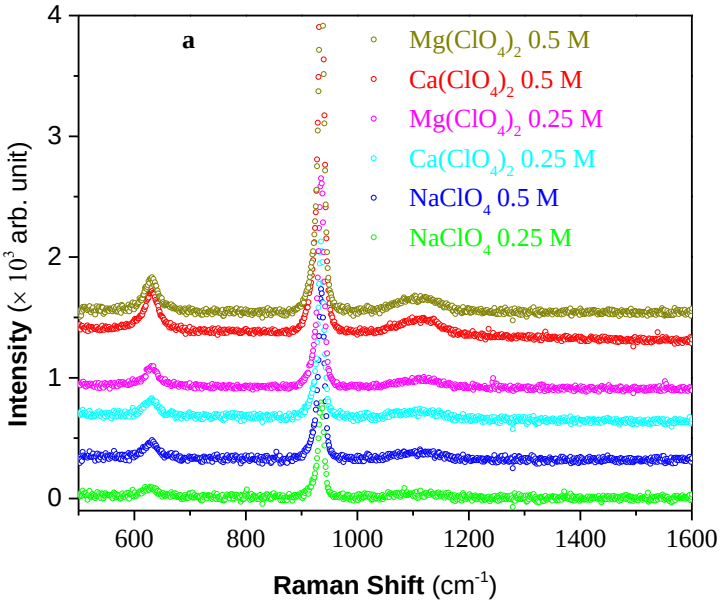

continued

Figure 3.5 Bulk Raman spectra of aqueous solutions at 0.25 and 0.5 M. (a) Perchlorate, (b) nitrate, and (c) sulfate. Spectra were uncorrected. The most intense peaks shown are the oxyanion symmetric stretch υ_1.

Figure 3.5 Continued

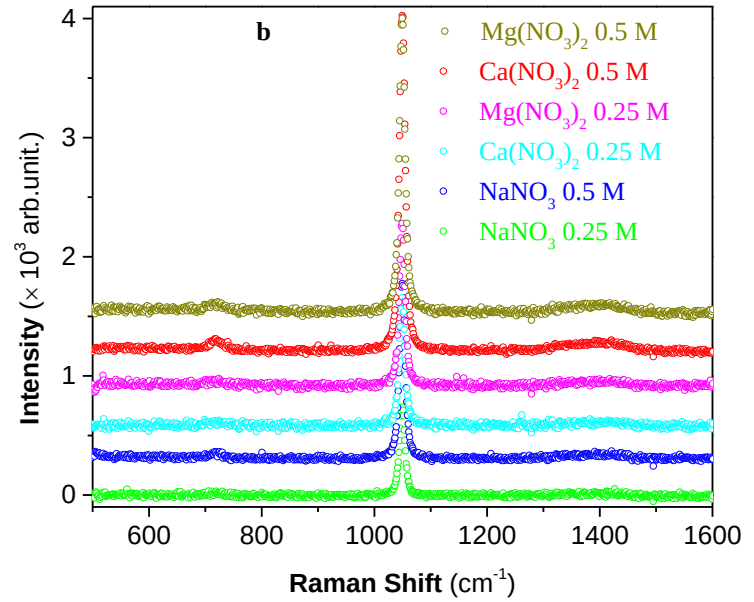

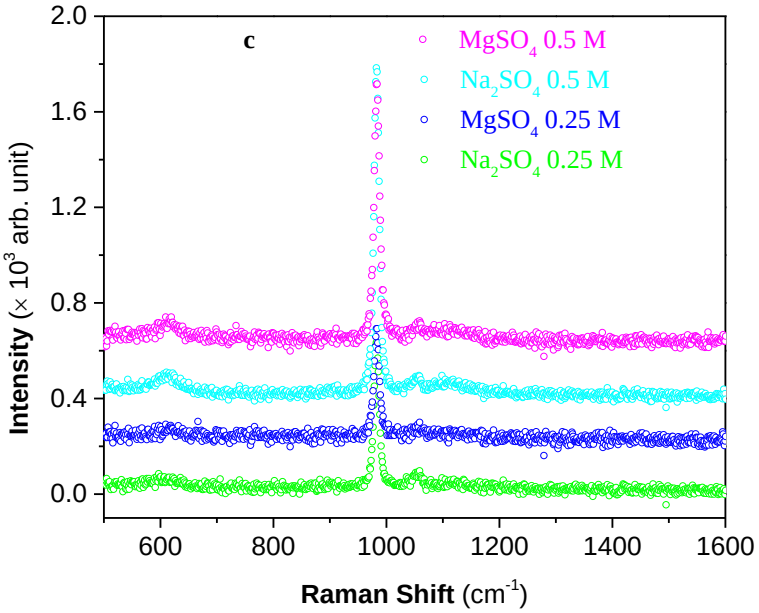

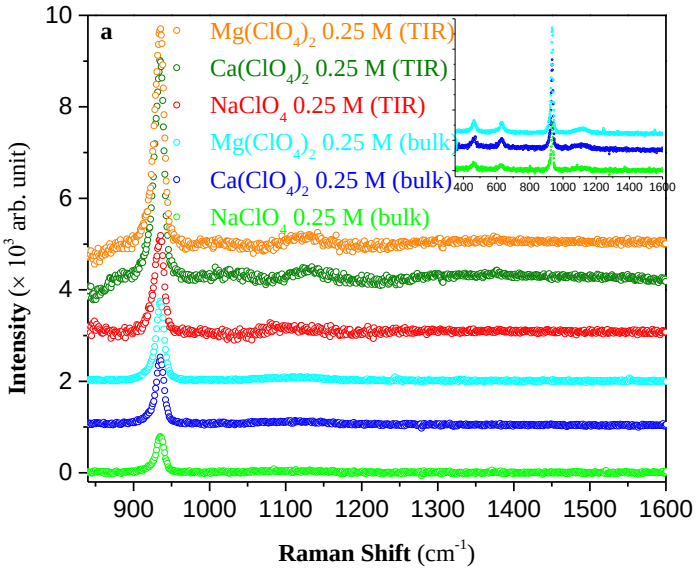

continued

Figure 3.6 Bulk and TIR-Raman spectra of aqueous solutions at 0.25 M. (a) Perchlorate, b) nitrate, and (c) sulfate. Insets show a broader spectral region of bulk spectra. Spectra were uncorrected. The most intense peaks shown are the oxyanion symmetric stretch υ_1 in the bulk and in the interfacial region. **However, caution needs to be taken when comparions of the peak positions between bulk Raman and TIR-Raman results are made; more careful calibrations for the two systems will be made to examine the shift of frequencies in the bulk and the interfacial region.**

Figure 3.6 continued

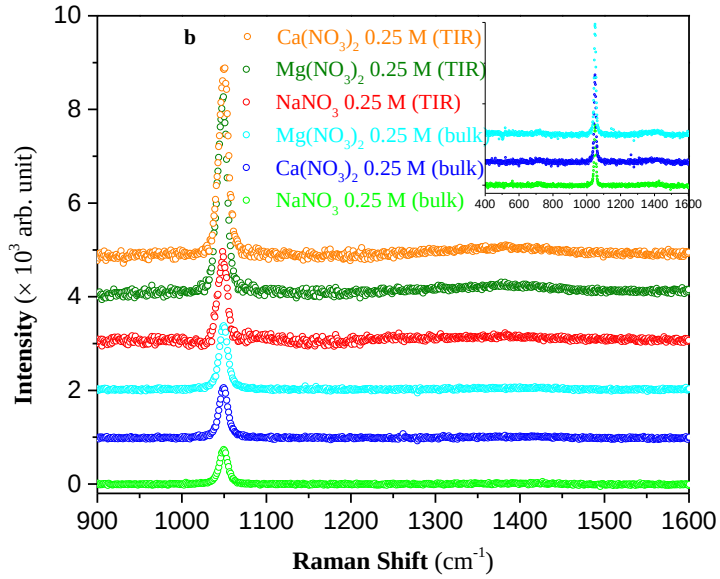

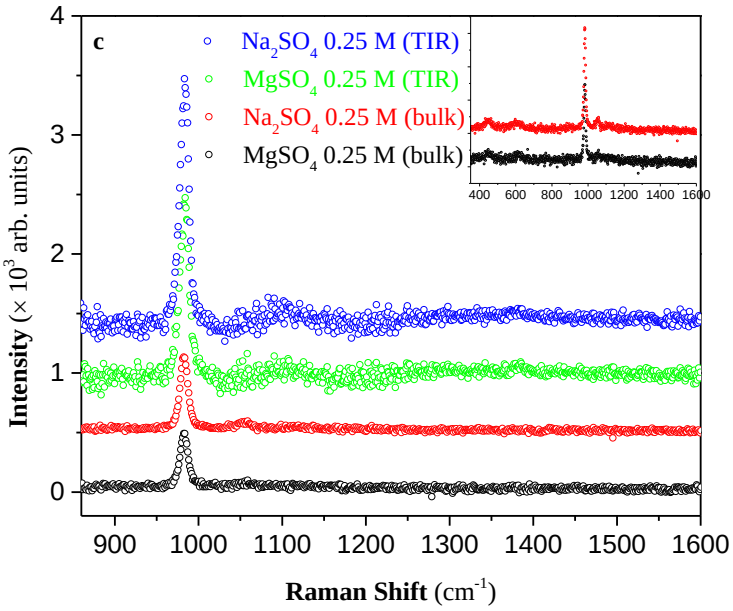

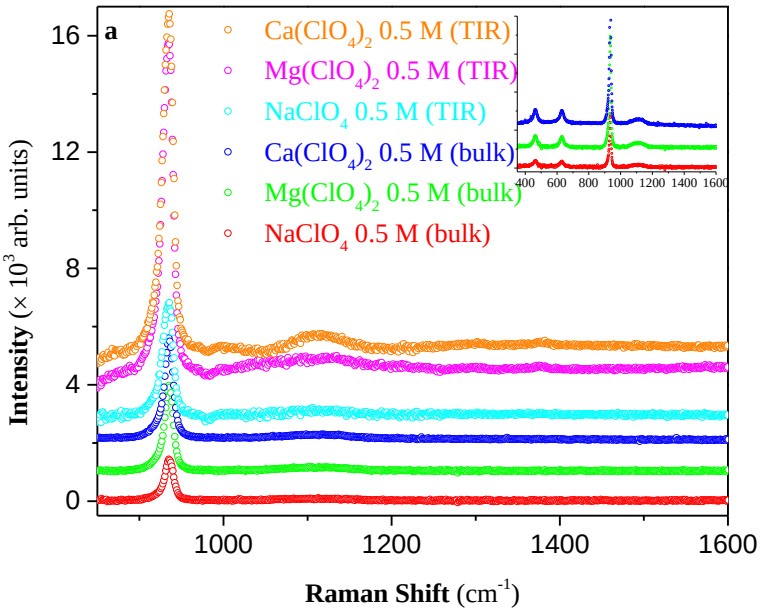

continued

Figure 3.7 Bulk and TIR-Raman spectra of aqueous solutions at 0.5 M. (a) Perchlorate, (b) nitrate, and (c) sulfate. Insets show a broader spectral region of bulk spectra. Spectra were uncorrected. The most intense peaks shown are the oxyanion symmetric stretch υ_1 in the bulk and in the interfacial region. **However, caution needs to be taken when comparions of the peak positions between bulk Raman and TIR-Raman results are made; more careful calibrations for the two systems will be made to examine the shift of frequencies in the bulk and the interfacial region.**

Figure 3.7 continued

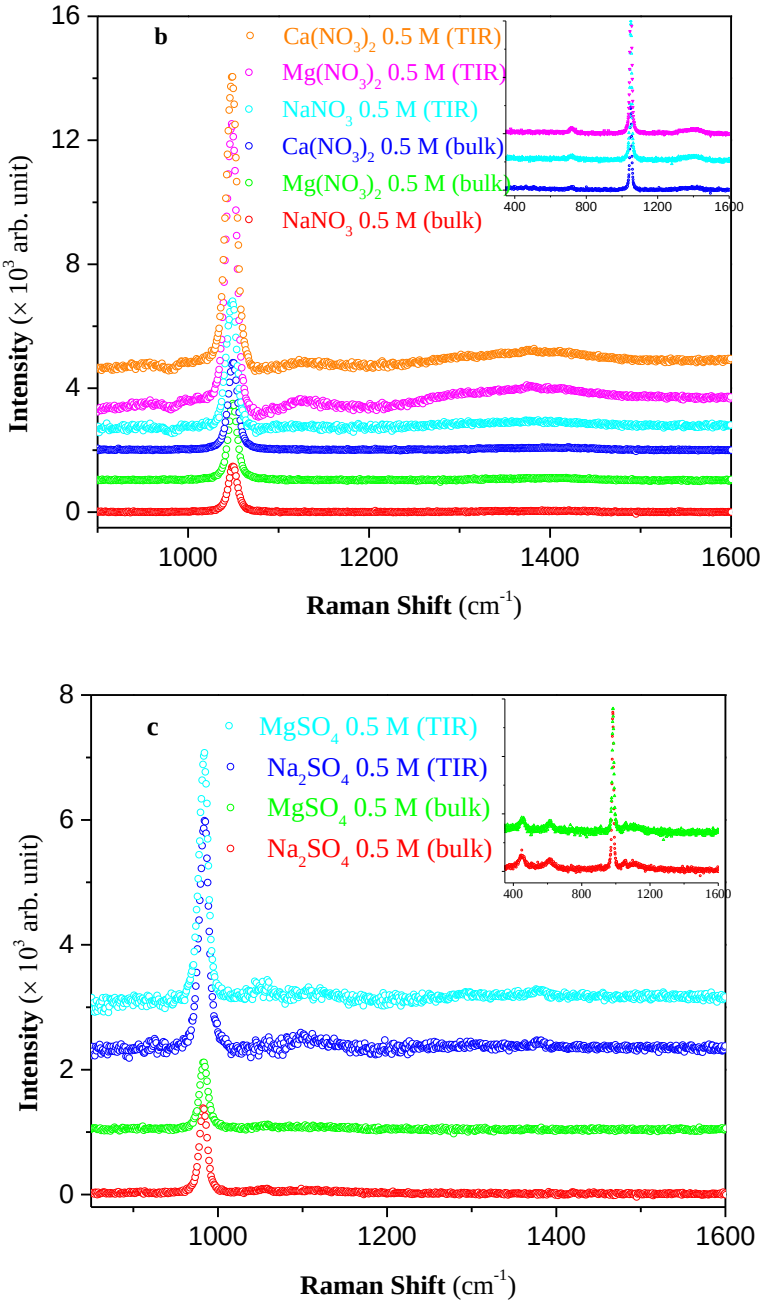

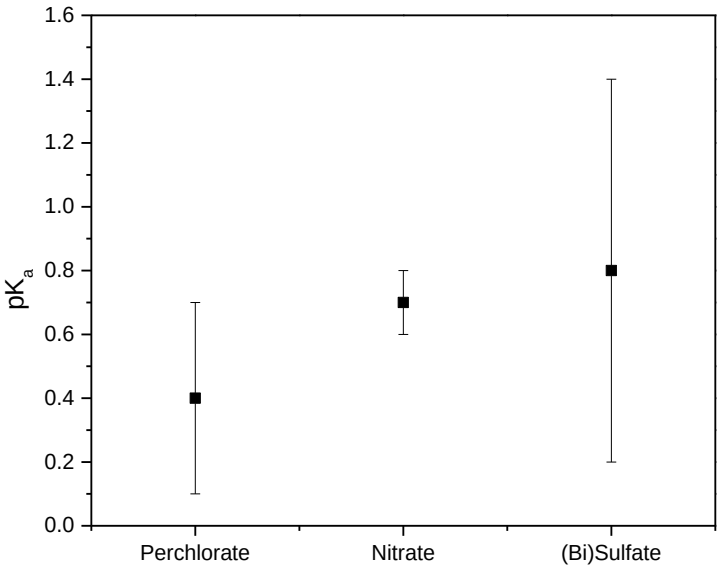

Figure 3.8 Acid dissociation constants at the water/silica interface for perchlorate, nitrate and bisulfate.

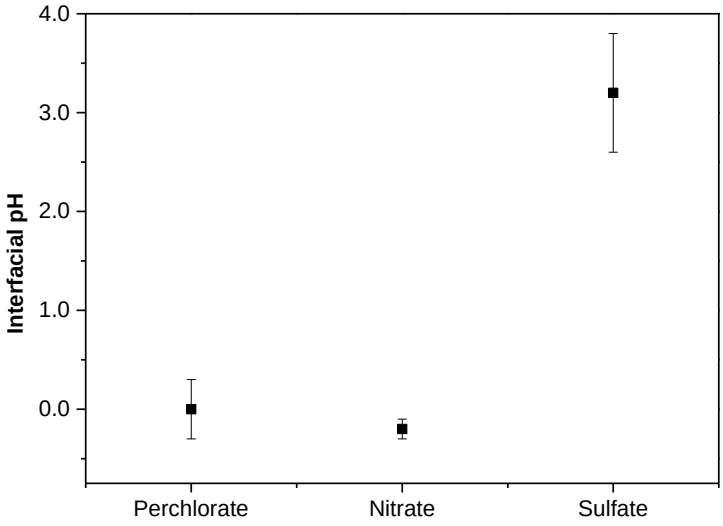

Figure 3.9 Interfacial pHs at the water/silica interface with perchlorate, nitrate and sulfate ions in the solution.

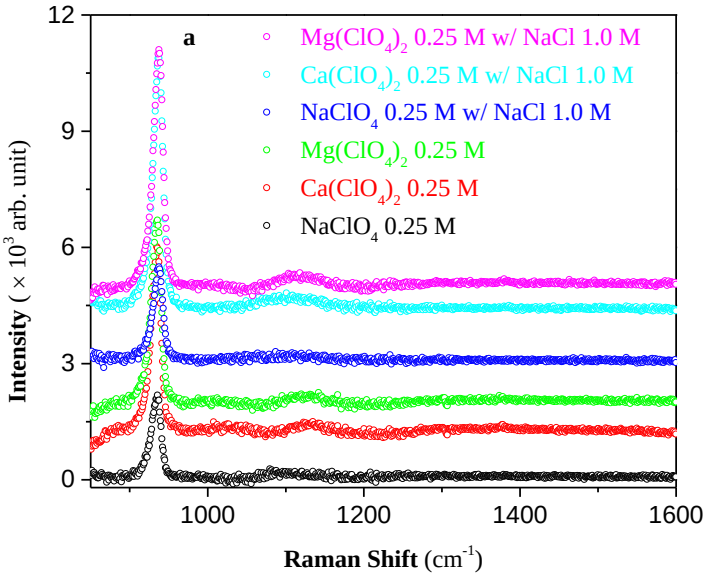

continued

Figure 3.10 TIR-Raman spectra of aqueous solutions at 0.25 M with and without 1.0 M NaCl as background electrolyte solution. (a) Perchlorate, (b) nitrate, and (c) sulfate. Raman intensity increases as 1.0 M NaCl is added for all 8 solutions.

Figure 3.10 continued

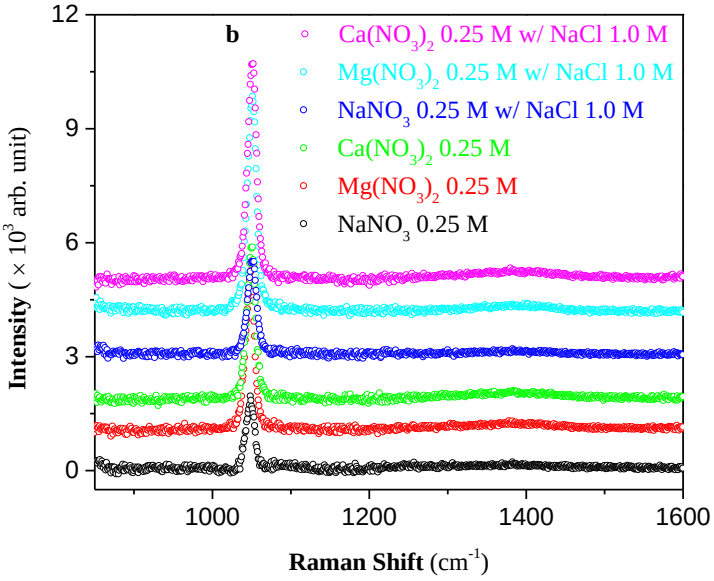

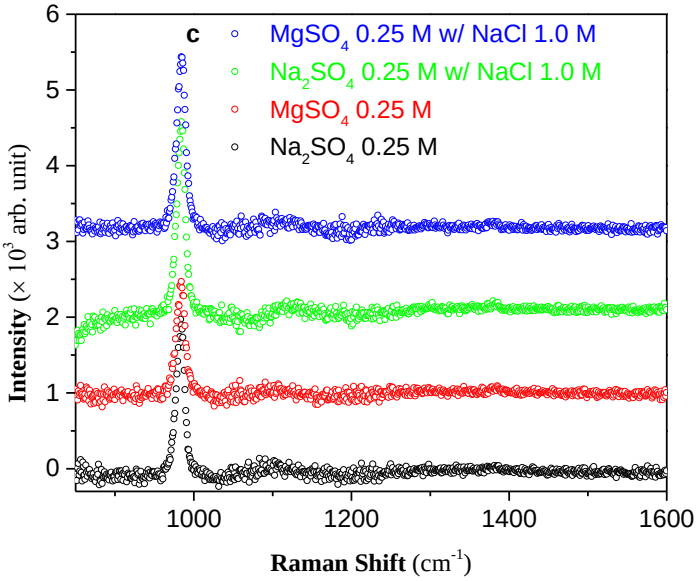

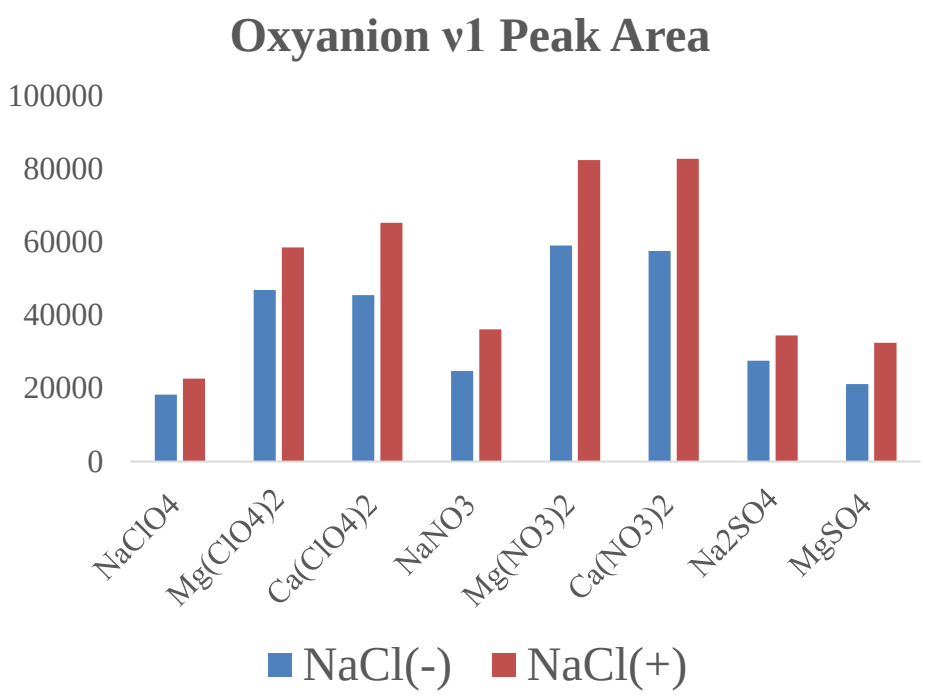

Figure 3.11 Peak areas of the oxyanion symmetric stretch v_1 mode for aqueous salt solutions with and without NaCl as background electrolytes. Peak areas of v_1 are consistently larger in the with NaCl case than without NaCl case.

Solution	Refractive Index (*n*)		Penetration Depth (*nm*)	
	NaCl(-)	*NaCl(+)*	*NaCl(-)*	*NaCl (+)*
H_2O	1.332	1.3425	134	147
$NaClO_4$	1.3342(1.3359)	1.3440(-)	137 (139)	149(-)
$Mg(ClO_4)_2$	1.3372(1.3419)	1.3465(-)	140 (146)	153(-)
$Ca(ClO_4)_2$	1.3378(1.3429)	1.3470(-)	141(148)	154(-)
$NaNO_3$	1.3348(1.3361)	1.3445(-)	137(139)	150(-)
$Mg(NO_3)_2$	1.3375(1.3420)	1.3470(-)	141(147)	154(-)
$Ca(NO_3)_2$	1.3382(1.3445)	1.3480(-)	141(150)	156(-)
Na_2SO_4	1.3371(1.3419)	1.3470(-)	140(146)	154(-)
$MgSO_4$	1.3384(1.3433)	1.3478(-)	142(148)	155(-)

Table 3.1 Refractive indices and associated penetration depth of perchlorate, nitrate and sulfate solutions at 0.25 and 0.5 M with (+) and without (-) NaCl as background electrolytes. Numbers outside of the parentheses are for 0.25 M and outside for 0.5 M.

Ionic strength (*M*)	**Debye Length** (*nm*)
0.001	13.59
0.25	0.35
0.75	0.20
1	0.18
1.5	0.14
2.75	0.11
3	0.10
5	0.08
6	0.07

Table 3.2 Debye length at different ionic strength calculated with Eqn. (35). ε_r used is that of water (78) and temperature T is at 298 K.

Chapter 4

Summary and Outlook

In this thesis, ion-specific effects were examined through the interaction with water in bulk and that at the silica/water interface. In bulk solutions, metal-water interaction were captured as metal-oxygen vibration. Magnesium cation interacts with water more strongly than both Ca and Na. In addition, in the low frequency region lies the stretching mode of hydrogen bonded water, where anions play a significant role in perturbing the water structure. A U-shaped trend of this stretch frequency indicates perchlorate and sulfate perturbs the water structure more significantly compared to chloride and nitrate. This agrees fairly well with the law of matching water affinities and shows that perchlorate and sulfate are indeed water structure-breaker and structure-maker, respectively.

Once a good understanding of ion interaction in bulk solution is reached, the interaction of ions at a charged surface was then investigated. Adsorption processes at the silica/aqueous interfaces are dictated by electrostatic interactions, which in the present study involves the transfer of protons from a surface silica site to an oxyanion. The acid constants specific to silica/aqueous interface or the interfacial pHs were extracted through spectral information by the Henderson-Hasselbach equation, assuming either one did not

differ significant from the bulk. Our results show that oxyanions modify the silica surface differently due to different oxyanion-interactions and specific chemical affinities to proton.

The role of background electrolytes is mainly to screen the surface sites from protonation to occur, or to squeeze ions into a more compact double layer. These two gave rise to the enhancement of the oxyanion modes. In addition, addition of charges certainly has increased Raman transition moment strength of these modes. A bulk measurement need to be performed to monitor whether this enhancement is surface specific or not. The surface concentration profiles for the three systems with respect to electrolyte concentration also need to be computed to have a better understanding on the integrated TIR- Raman intensity, shown in eqn. (36). **In addition, different cations have different abilities of screening a charged surface and this difference has not yet been examined in this study (Mg^{2+}, Ca^{2+} and Na^{+}).**

The study of ions remains important in many scientific areas because of the fundamentality of the subject and its great potential to applications. A broader investigation can be conducted in the future, such as multivalent cation−water interaction. For example, the trivalent cations are not examined here due to the complexity of the ions themselves. Iron(III) for example, exhibits amphoterism as it can accept or donate a proton. Also water can be considered as a ligand, and charge transfer process in the metal-ligand system can easily complicate the study. Due to the electronic processes in these systems, a different technique such as some electronic spectroscopy may be employed to avoid the complication of different optical phenomena such as absorption

and fluorescence. Another set of experiments can be to study a series of organic ions such as acetates with different chain lengths (methyl acetate, ethyl acetate, etc.) or the effect of a different solvent, (water, methanol, dimethylsulfoxide, etc.). At the surface, adsorption onto other mineral substrates that are of geochemical importance (e.g. goethite and hematite) is also fairly intriguing since the central atom is now a metal. The interaction of oxyanion with the charged surface will differ greatly from the silica surface. The chemistry will be altered: inner-sphere complexes are likely to occur instead of protonation. Therefore, TIR-Raman investigation on these systems will certainly shed light in the field of geochemical adsorption. Again, a theoretical model on ion-water interactions at the surface vs. bulk is in urgent need to provide fundamental understanding to confirm our experimental findings.

References

1. W. Kunz, J. Henle and B. W. Ninham, *Curr. Opin. Colloid In.*, 2004, 9, 19.
2. N. N. Casillas-Ituarte, K. M. Callahan, C. Y. Tang, X. K. Chen, M. Roeselova, D. J. Tobias and H. C. Allen, *P. Natl. Acad. Sci. USA*, 2010, 107, 6616.
3. Y.-L. Liu, I. C. Tsai, C.-W. Chang, Y.-F. Liao, G.-Y. Liu and H.-C. Hung, *Plos One*, 2013, 8, e51660.
4. M. E. Maguire and J. A. Cowan, *Biometals*, 2002, 15, 203.
5. A. M. Pyle, *J. Biol. Inorg. Chem.*, 2002, 7, 679.
6. P. J. Romero and R. Whittam, *J. Physiol.-London*, 1971, 214, 481.
7. S. Taneva, T. McEachren, J. Stewart and K. M. W. Keough, *Biochemistry-US*, 1995, 34, 10279.
8. R. J. P. Williams, in *Calcium: A Matter of Life or Death*, eds. J. Krebs and M. Michalak, 2007, vol. 41, pp. 23-48.
9. J. B. J. Finlayson-Pitts; J. N. Pitts, *Chemistry of the Upper and Lower Atmosphere: Theory, Experiments and Applications*, Academic Press, San Diego, CA, 2000.
10. S. Borrmann, S. Solomon, J. E. Dye, D. Baumgardner, K. K. Kelly and K. R. Chan, *J Geophys. Res-Atmos.*, 1997, 102, 3639.
11. M. O. Andreae and P. J. Crutzen, *Science*, 1997, 276, 1052.
12. P. K. Dasgupta, P. K. Martinelango, W. A. Jackson, T. A. Anderson, K. Tian, R. W. Tock and S. Rajagopalan, *Environ. Sci. Technol.*, 2005, 39, 1569.
13. J. Kapitan, M. Dracinsky, J. Kaminsky, L. Benda and P. Bour, *J. Phys. Chem. B*, 2010, 114, 3574.
14. K. D. Collins, *Methods*, 2004, 34, 300.
15. Y. Marcus, *Chem. Rev.*, 1988, 88, 1475.
16. Y. Marcus, *Chem. Rev.*, 2009, 109, 1346.
17. H. Ohtaki and T. Radnai, *Chem. Rev.*, 1993, 93, 1157.
18. Y. S. Badyal, A. C. Barnes, G. J. Cuello and J. M. Simonson, *J. Phys. Chem. A*, 2004, 108, 11819.
19. M. I. Bernal-Uruchurtu and I. Ortega-Blake, *J. Phys. Chem. A*, 1999, 103, 884.
20. R. Caminiti, P. Cucca, M. Monduzzi, G. Saba and G. Crisponi, *J. Chem. Phys.*, 1984, 81, 543.
21. R. Caminiti, G. Licheri, G. Paschina, G. Piccaluga and G. Pinna, *J. Chem. Phys.*, 1980, 72, 4522.
22. R. Caminiti, G. Licheri, G. Paschina, G. Piccaluga and G. Pinna, *Z. Naturforsch. A*, 1980, 35, 1361.

23. R. Caminiti, G. Licheri, G. Piccaluga and G. Pinna, *Chem. Phys. Lett.*, 1979, 61, 45.
24. O. Carugo, K. Djinovic and M. Rizzi, *J. Chem. Soc. Dalton*, 1993, DOI: 10.1039/dt9930002127, 2127.
25. S. Cummings, J. E. Enderby and R. A. Howe, *J. Phys. C Solid State*, 1980, 13, 1.
26. W. Dietz, W. O. Riede and K. Heinzinger, *Z. Naturforsch. A*, 1982, 37, 1038.
27. F. M. Floris, M. Persico, A. Tani and J. Tomasi, *Chem. Phys. Lett.*, 1994, 227, 126.
28. J. L. Fulton, S. M. Heald, Y. S. Badyal and J. M. Simonson, *J. Phys. Chem. A*, 2003, 107, 4688.
29. N. A. Hewish, G. W. Neilson and J. E. Enderby, *Nature (London)*, 1982, 297, 138.
30. R. W. Impey, P. A. Madden and I. R. McDonald, *J Phys. Chem.*, 1983, 87, 5071.
31. F. C. Lightstone, E. Schwegler, R. Q. Hood, F. Gygi and G. Galli, *Chem. Phys. Lett.*, 2001, 343, 549.
32. R. Mancinelli, A. Botti, F. Bruni, M. A. Ricci and A. K. Soper, *J. Phys. Chem. B*, 2007, 111, 13570.
33. F. T. Marchese and D. L. Beveridge, *J. Am. Chem. Soc.*, 1984, 106, 3713.
34. G. D. Markham, J. P. Glusker and C. W. Bock, *J. Phys. chem. B*, 2002, 106, 5118.
35. M. Mezei and D. L. Beveridge, *J. Chem. Phys.*, 1981, 74, 6902.
36. N. Ohtomo and K. Arakawa, *B. Chem. Soc. Jpn.*, 1980, 53, 1789.
37. G. Palinkas, T. Radnai and F. Hajdu, *Z. Naturforsch. A*, 1980, 35, 107.
38. M. M. Probst, T. Radnai, K. Heinzinger, P. Bopp and B. M. Rode, *J. Phys. Chem.*, 1985, 89, 753.
39. A. Tongraar, K. R. Liedl and B. M. Rode, *J. Phys. Chem. A*, 1998, 102, 10340.
40. J. A. White, E. Schwegler, G. Galli and F. Gygi, *J. Chem. Phys.*, 2000, 113, 4668.
41. T. Yamaguchi, S. Hayashi and H. Ohtaki, *Inorg. Chem.*, 1989, 28, 2434.
42. E. Hawlicka and M. Rybicki, in *Molecular Dynamics -Theoretical Developments and Applications in Nanotechnology and Energy*, ed. L. Wang, Intech, New York, 2012, ch. 19.
43. D. Di Tommaso and N. H. de Leeuw, *Phys. Chem. Chem. Phys.*, 2010, 12, 894.
44. H. Kanno, *J. Phys. Chem.*, 1988, 92, 4232.
45. T. G. Chang and D. E. Irish, *J. Phys. Chem.*, 1973, 77, 52.
46. A. R. Davis and B. G. Oliver, *J. Phys. Chem.*, 1973, 77, 1315.
47. Y. Marcus and G. Hefter, *Chem. Rev.*, 2006, 106, 4585.
48. J. Mink, C. Nemeth, L. Hajba, A. Sandstrom and P. L. Goggin, *J. Mol. Struct.*, 2003, 661, 141.
49. Z. Nickolov, I. Ivanov, G. Georgiev and D. Stoilova, *J. Mol. Struct.*, 1996, 377, 13.
50. F. Quiles and A. Burneau, *Vib. Spectrosc.*, 1998, 16, 105-117.
51. W. W. Rudolph, G. Irmer and G. T. Hefter, *Phys. Chem. Chem. Phys.*, 2003, 5, 5253.
52. F. Rull, C. Balarew, J. L. Alvarez, F. Sobron and A. Rodriguez, *J. Raman Spectrosc.*, 1994, 25, 933.

53. V. Tomisic and V. Simeon, *Phys. Chem. Chem. Phys.*, 2000, 2, 1943.
54. A. Wahab, S. Mahiuddin, G. Hefter, W. Kunz, B. Minofar and P. Jungwirth, *J. Phys. Chem. B*, 2005, 109, 24108.
55. L. Y. Wang, Y. H. Zhang and L. J. Zhao, *J. Phys. Chem. A*, 2005, 109, 609-614.
56. M. Xu, J. P. Larentzos, M. Roshdy, L. J. Criscenti and H. C. Allen, *Phys. Chem. Chem. Phys.*, 2008, 10, 4793.
57. Y. H. Zhang, M. Y. Choi and C. K. Chan, *J. Phys. Chem. A*, 2006, 110, 7516-7516.
58. M. Peleg, *J. Phys. Chem.*, 1972, 76, 1019.
59. Y. H. Zhang, M. Y. Choi and C. K. Chan, *J. Phys. Chem. A*, 2006, 110, 7516.
60. K. M. Callahan, N. N. Casillas-Ituarte, M. Xu, M. Roeselova, H. C. Allen and D. J. Tobias, *J. Phys. Chem. A*, 2010, 114, 8359.
61. Chatterj.Rm, W. A. Adams and A. R. Davis, *J. Phys. Chem.*, 1974, 78, 246.
62. F. P. Daly, D. R. Kester and C. W. Brown, *J. Phys. Chem.*, 1972, 76, 3664.
63. C. C. Pye and W. W. Rudolph, *J. Phys. Chem. A*, 1998, 102, 9933.
64. C. I. Ratcliffe and D. E. Irish, *Can. J. Chem.*, 1984, 62, 1134.
65. W. Kunz, *Pure Appl. Chem.*, 2006, 78, 1611.
66. W. Kunz, *Curr. Opin. Colloid In.*, 2010, 15, 34.
67. A. Chatterjee, M. K. Dixit and B. L. Tembe, *J. Phys. Chem. A*, 2013, 117, 8703.
68. F. Bruni, S. Imberti, R. Mancinelli and M. A. Ricci, *J. Chem. Phys.*, 2012, 136, 064520-064521.
69. A. A. Chialvo and J. M. Simonson, *J. Chem. Phys.*, 2003, 119, 8052.
70. E. Owczarek, M. Rybicki and E. Hawlicka, *J. Phys. Chem. B*, 2007, 111, 14271.
71. D. M. Carey and G. M. Korenowski, *J. Chem. Phys.*, 1998, 108, 2669.
72. R. Lafont, *Cr. Hebd. Acad. Sci.*, 1957, 244, 1481.
73. W. W. Rudolph and G. Irmer, *Dalton T.*, 2013, 42, 3919.
74. R. Buchner, T. Chen and G. Hefter, *J. Phys. Chem. B*, 2004, 108, 2365.
75. F. Rull and H. Ohtaki, *Spectrochim. Acta A*, 1997, 53, 643.
76. F. Rull and F. Sobron, *J. Raman Spectrosc.*, 1994, 25, 693.
77. M. H. Brooker and C. H. Huang, *Can. J. Chem.*, 1980, 58, 168.
78. C. H. Huang and M. H. Brooker, *Chem. Phys. Lett.*, 1976, 43, 180.
79. G. E. Walrafen, *J. Chem. Phys.*, 1964, 40, 3249.
80. G. E. Walrafen, Y. C. Chu and G. J. Piermarini, *J. Phys. Chem.*, 1996, 100, 10363.
81. G. E. Walrafen, *J. Chem. Phys.*, 1966, 44, 1546.
82. M. Xu, PhD, The Ohio State University, 2008.
83. H. Kanno and J. Hiraishi, *J. Raman Spectrosc.*, 1987, 18, 157.
84. M. Heyden, J. Sun, S. Funkner, G. Mathias, H. Forbert, M. Havenith and D. Marx, *P. Natl. Acad. Sci. USA*, 2010, 107, 12068.
85. D. Harris and M. Bertolucci, *Symmetry and Spectroscopy: An Introduction to Vibrational and Electronic Spectroscopy*, Dover Publications, New York, 1989.
86. R. J. Capwell, *Chem. Phys. Lett.*, 1972, 12, 443.
87. H. Sano, H. Miyaoka, T. Kuze, H. Mori, G. Mizutani, N. Otsuka and M. Terano, *Surf. Sci.*, 2002, 502, 70.

88. S. Funkner, G. Niehues, D. A. Schmidt, M. Heyden, G. Schwaab, K. M. Callahan, D. J. Tobias and M. Havenith, *J. Am. Chem. Soc.*, 2012, 134, 1030.
89. K. Cabrera, *J. Sep. Sci.*, 2004, 27, 843.
90. C. R. Kurkjian, J. T. Krause and U. C. Paek, *J. Phys.-Paris*, 1982, 43, 585.
91. G. A. Somorjai, H. Frei and J. Y. Park, *J. Am. Chem. Soc.*, 2009, 131, 16589.
92. Q.-Y. Tong and U. Gosele, *Semiconductor Wafer Bonding: Science and Technology*, John Wiley & Sons, New York, 1999.
93. N. N. Casillas-Ituarte and H. C. Allen, *Chem. Phys. Lett.*, 2009, 483, 84.
94. P. K. Gupta and M. Meuwly, *Faraday Discuss.*, 2013, 167, 329.
95. O. Isaienko and E. Borguet, *Langmuir*, 2013, 29, 7885.
96. T. S. Mahadevan and S. H. Garofalini, *J. Phys. Chem. C*, 2008, 112, 1507.
97. S. Nangia and B. J. Garrison, *J. Phys. Chem. A*, 2008, 112, 2027.
98. M. Sulpizi, M.-P. Gaigeot and M. Sprik, *J. Chem. Theory Comput.*, 2012, 8, 1037.
99. A. F. Wallace, G. V. Gibbs and P. M. Dove, *J. Phys. Chem. A*, 2010, 114, 2534.
100. W. Stumm, *Colloid. Surface. A*, 1997, 120, 143.
101. P. M. Dove and J. D. Rimstidt, in *Silica: Physical Behavior, Geochemistry and Materials Applications*, 1994, vol. 29, p. 259.
102. J. D. Rimstidt and H. L. Barnes, *Geochim. Cosmochim. Ac.*, 1980, 44, 1683.
103. T. A. Michalske and S. W. Freiman, *Nature*, 1982, 295, 511.
104. K. L. Geisinger, G. V. Gibbs and A. Navrotsky, *Phys. Chem. Miner.*, 1985, 11, 266.
105. A. C. Lasaga, *Atomic Treatment of Mineral-Water Surface-Reactions*, 1990.
106. C. Cao, Y. He, J. Torras, E. Deumens, S. B. Trickey and H.-P. Cheng, *J. Chem. Phys.*, 2007, 126, 211101-211101.
107. M. H. Du, A. Kolchin and H. P. Cheng, *J. Chem. Phys.*, 2004, 120, 1044.
108. Q. Du, E. Freysz and Y. R. Shen, *Phys. Rev. Lett.*, 1994, 72, 238.
109. Y. C. Ma, A. S. Foster and R. M. Nieminen, *J. Chem. Phys.*, 2005, 122, 144709.
110. C. Mischler, J. Horbach, W. Kob and K. Binder, *J. Phys.-Condens. Mat.*, 2005, 17, 4005.
111. P. K. Schindler, H.R., *Helv. Chim. Acta*, 1968, 51, 1781.
112. K. Leung, I. M. B. Nielsen and L. J. Criscenti, *J. Am. Chem. Soc.*, 2009, 131, 18358.
113. M. Kosmulski, *Ber. Bunsen. Phys. Chem.*, 1994, 98, 1062.
114. V. Ostroverkhov, G. A. Waychunas and Y. R. Shen, *Chem. Phys. Lett.*, 2004, 386, 144.
115. V. Ostroverkhov, G. A. Waychunas and Y. R. Shen, *Phys. Rev. Lett.*, 2005, 94, 046102.
116. M. Dishon, O. Zohar and U. Sivan, *Langmuir*, 2011, 27, 12977.
117. P. M. Dove, *Geochim. Cosmochim. Ac.*, 1999, 63, 3715.
118. P. M. Dove and C. M. Craven, *Geochim. Cosmochim. Ac.*, 2005, 69, 4963.
119. Z. Yang, Q. Li and K. C. Chou, *J. Phys. Chem. C*, 2009, 113, 8201.
120. K. F. Hayes and J. O. Leckie, *J. Colloid Interf. Sci.*, 1987, 115, 564-572.
121. M. A. Malati and S. F. Estefan, *J. Colloid Interf. Sci.*, 1966, 22, 306.
122. N. Sahai and D. A. Sverjensky, *Geochim. Cosmochim. Ac.*, 1997, 61, 2827.

123. J. Burgess, *Ions in Solution*, Halsted Press, New York, 1988.
124. A. M. Jubb, D. Verreault, R. Posner, L. J. Criscenti, L. E. Katz and H. C. Allen, *J. Colloid Interf. Sci.*, 2013, 400, 140.
125. B. Bharti, J. Meissner, S. H. L. Klapp and G. H. Findenegg, *Soft Matter*, 2014, 10, 718.
126. H.-C. Chang, T.-C. Hung, S.-C. Chang, J.-C. Jiang and S. H. Lin, *J. Phys. Chem. C*, 2011, 115, 11962.
127. K. Wandelt, in *Surface and Interface Science: Concepts and Methods*, ed. K. Wandelt, John Wiley & Sons, 2012, vol. 1.
128. D. A. Woods and C. D. Bain, *Soft Matter*, 2014, 10, 1071.
129. P. L. Stiles, J. A. Dieringer, N. C. Shah and R. R. Van Duyne, in *Annu. Rev. Anal. Chem.*, 2008, vol. 1, p. 601.
130. M. Milosevic, John Wiley & Sons, USA, 2012.
131. A. D. Wiesner, L. E. Katz and C. C. Chen, *J. Colloid Interf. Sci.*, 2006, 301, 329.
132. C. Pitot, *Abbe Zeiss Refractomer*.
133. L. Weiss, A. Tazibt, A. Tidu and M. Aillerie, *J. Chem. Phys.*, 2012, 136, 124201.
134. I. H. Malitson, *J. Opt. Soc. Am.*, 1965, 55, 1205-&.
135. R. L. Frost, D. W. James, R. Appleby and R. E. Mayes, *J. Phys. Chem.*, 1982, 86, 3840.
136. H. D. Lutz, R. A. Becker, W. Eckers, B. G. Holscher and H. J. Berthold, *Spectrochim. Acta A*, 1983, 39, 7.
137. H. D. Lutz, R. A. Becker, B. G. Kruska and H. J. Berthold, *Spectrochim. Acta A*, 1979, 35, 797.
138. J. P. O'Reilly, C. P. Butts, I. A. I'Anson and A. M. Shaw, *J. Am. Chem. Soc.*, 2005, 127, 1632.
139. O. Gershevitz, A. Osnis and C. N. Sukenik, *Isr. J. Chem.*, 2005, 45, 321.
140. C. E. L. Myhre, D. H. Christensen, F. M. Nicolaisen and C. J. Nielsen, *J. Phys. Chem. A*, 2003, 107, 1979.
141. D. Dzombak and F. Morel, *Surface Complexation Modeling: Hydrous Ferric Oxide*, John Wiley & Sons, USA, 1990.
142. P. Schindler, *Osterr. Chem. Z.*, 1985, 86.
143. L. Sigg and W. Stumm, *Colloid. Surface.*, 1981, 2, 101.
144. C. Brett; and A. Brett, *Electrochemistry: Principles, Methods, and Applications*, Oxford University Press, USA, 1993.
145. A. O. Kivioja, A.-S. Jaaskelainen, V. Ahtee and T. Vuorinen, *Vib. Spectrosc.*, 2012, 61, 1.
146. H. Zhang, A. A. Hassanali, Y. K. Shin, C. Knight and S. J. Singer, *J. Chem. Phys.*, 2011, 134, 024705.

APPENDIX A.

Fitted Raman Spectra of Magnesium and Calcium Salt Solutions

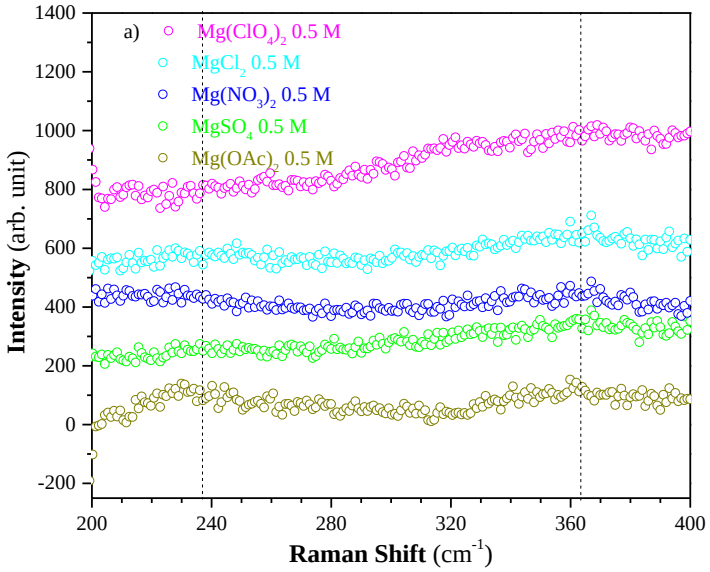

continued

Figure A1-4. Difference Raman spectra of magnesium and calcium salts in the low frequency region. Spectra of 2.0 M solutions are fitted with Gaussian functions. Acetate spectra are included, yet caution needs to take to compare acetate with other anions due to organic nature of acetate ions.

Figure A1-4. continued

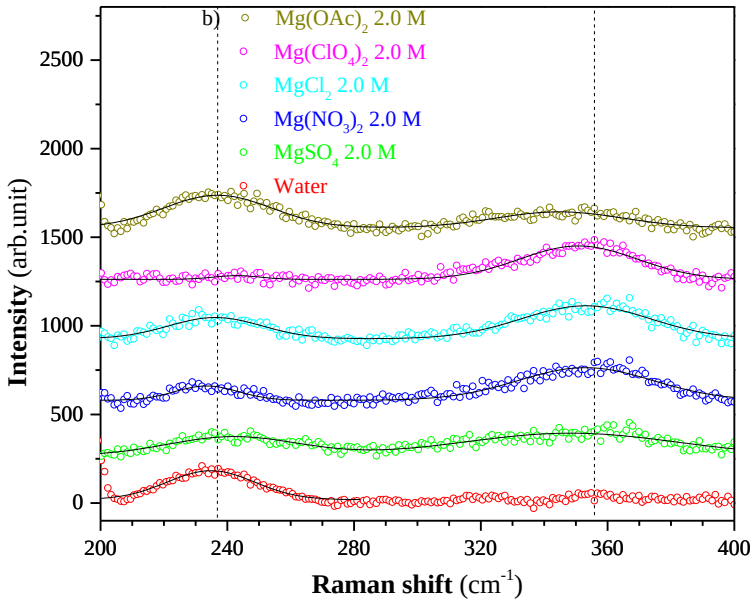

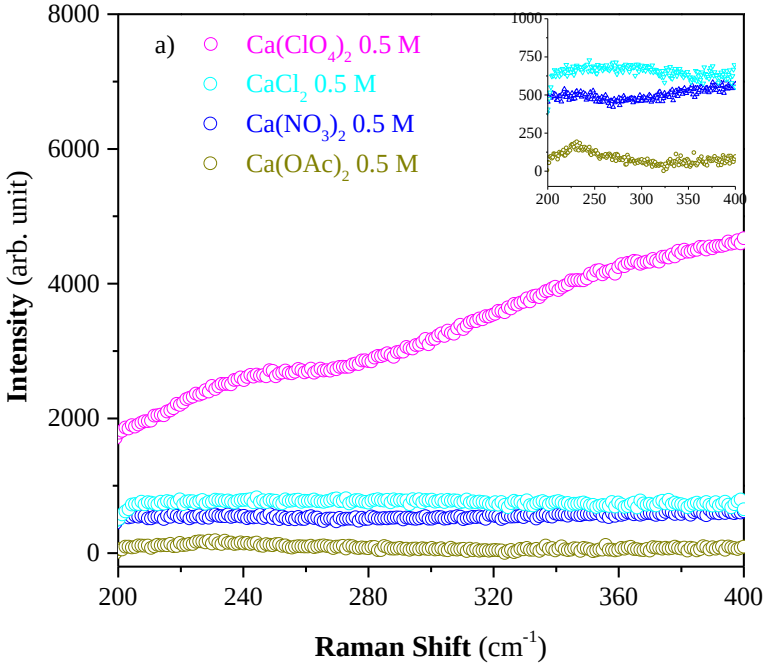

continued

Figure A1-4. continued

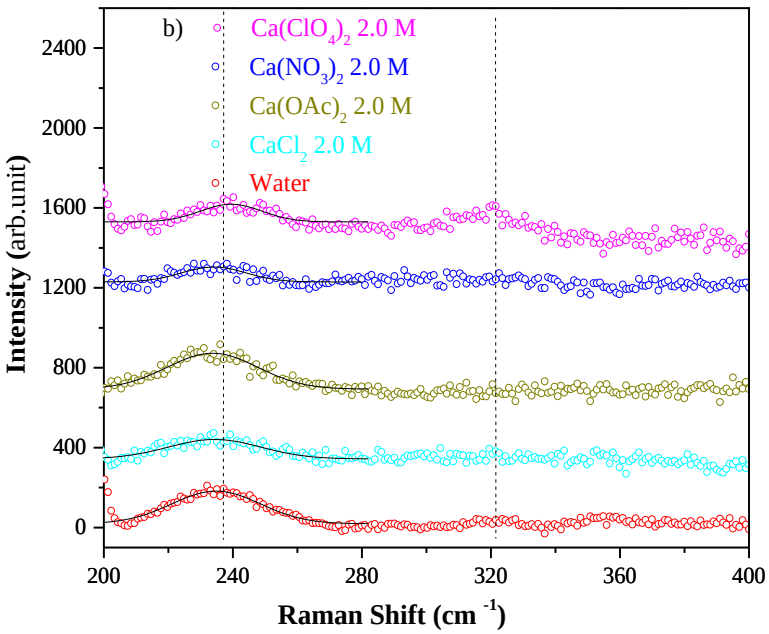

APPENDIX B.

Comparison of Low Frequency Raman Spectra of Mg and Na Salt Solutions

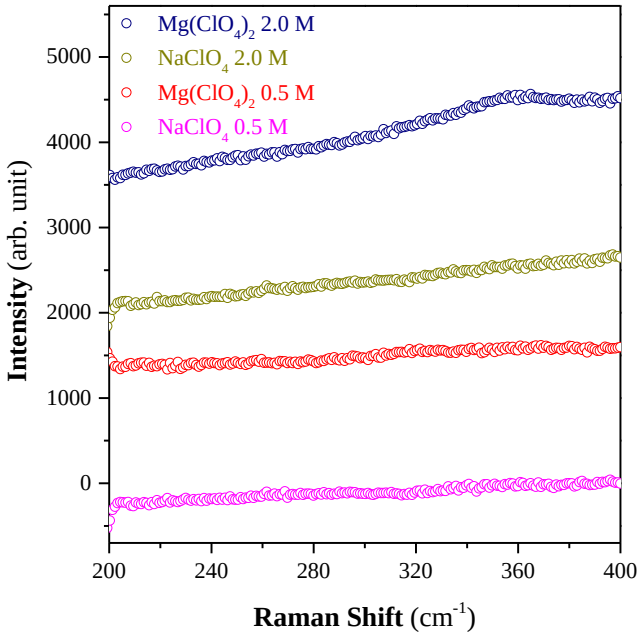

continued

Figure B1-4. Difference Raman spectra of magnesium and sodium salts in the low frequency region. Perchlorate, chloride, nitrate and sulfate are included. Na-O stretch is not shown to be in this region. In addition, stretching mode of hydrogen bonded water is not enhanced by Mg^{2+}, but not Na^{+}.

Figure B1-4. continued

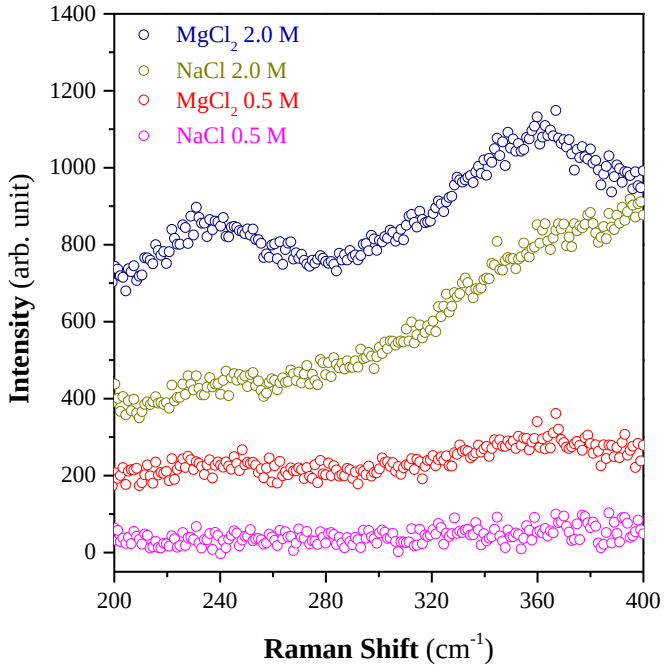

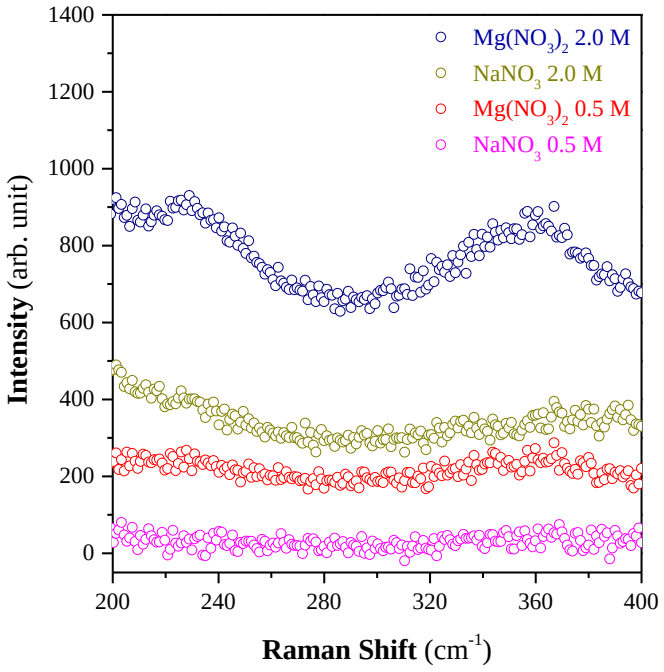

continued

Figure B1-4. continued

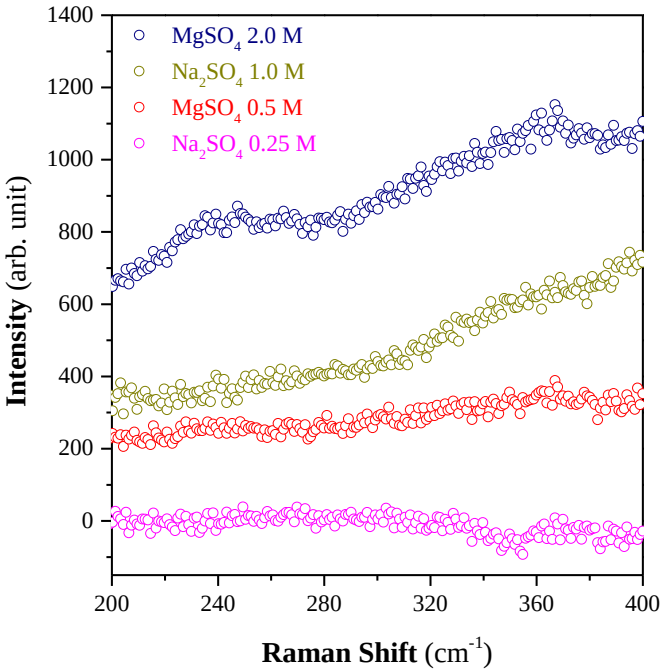

APPENDIX C.

Oxyanion Modes in Neat Water, 1.0 M NaCl and 1.5 M NaCl

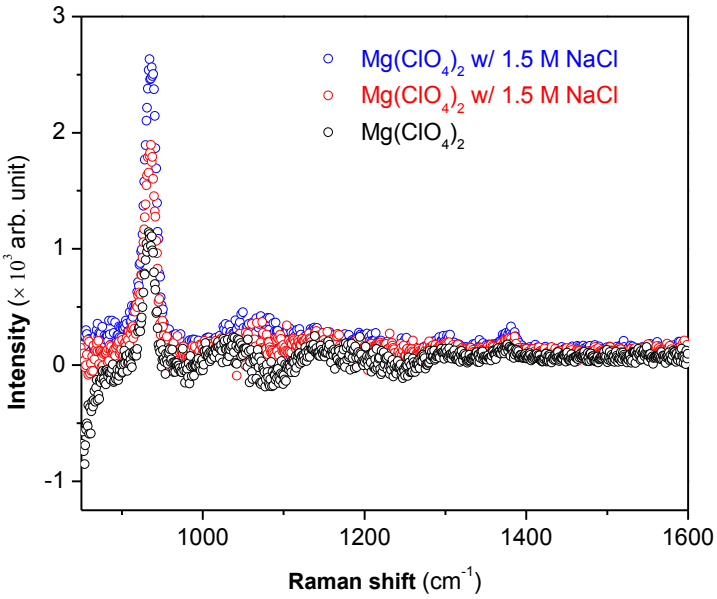

continued

Figure C1-8. Raman spectra of magnesium, calcium and sodium oxyanion salt solutions at the silica-water interface. The most intensity peak of each spectrum is the oxyanion symmetric stretch ν_1. Clearly, the peak increases as the concentration of background electrolyte NaCl increases.

Figure C1-8. continued

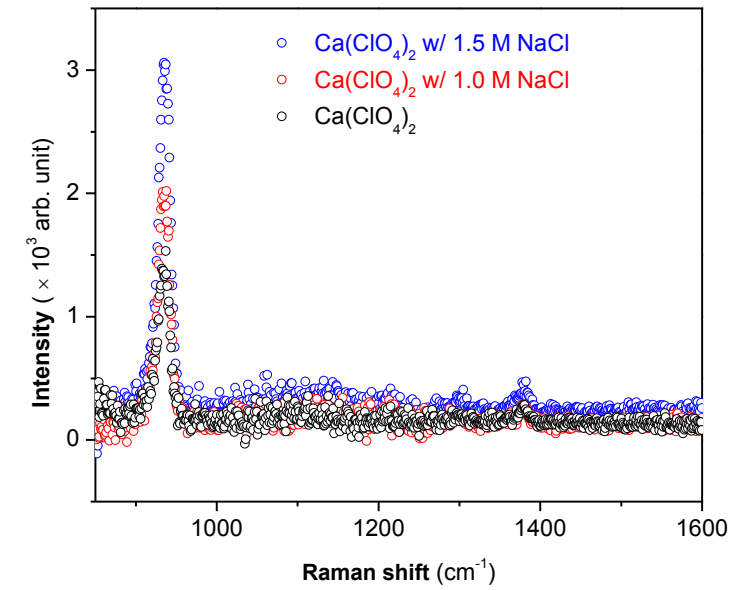

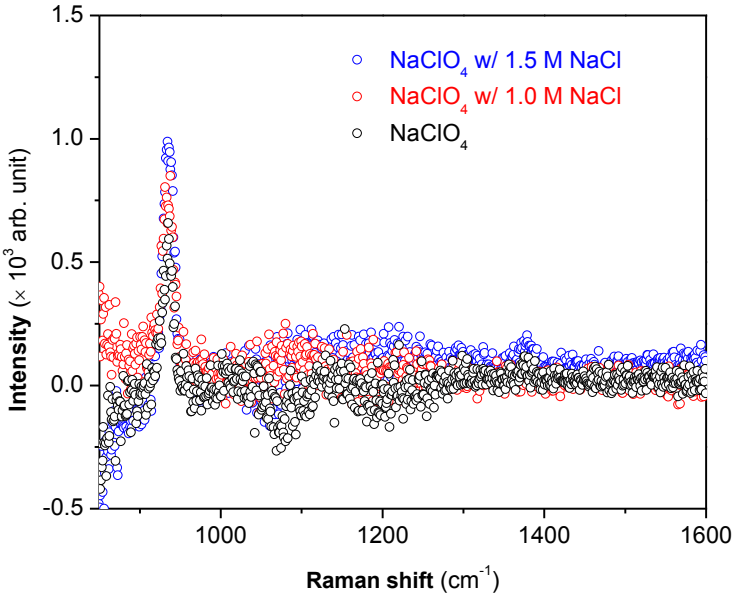

continued

Figure C1-8. continued

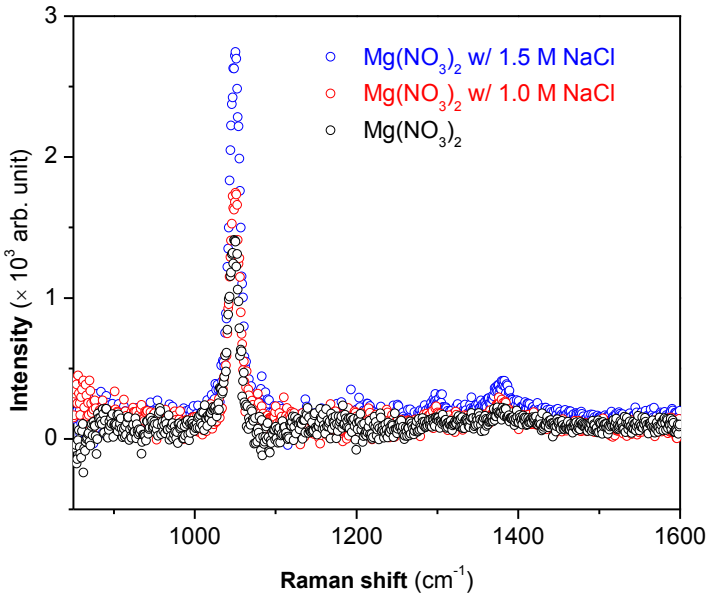

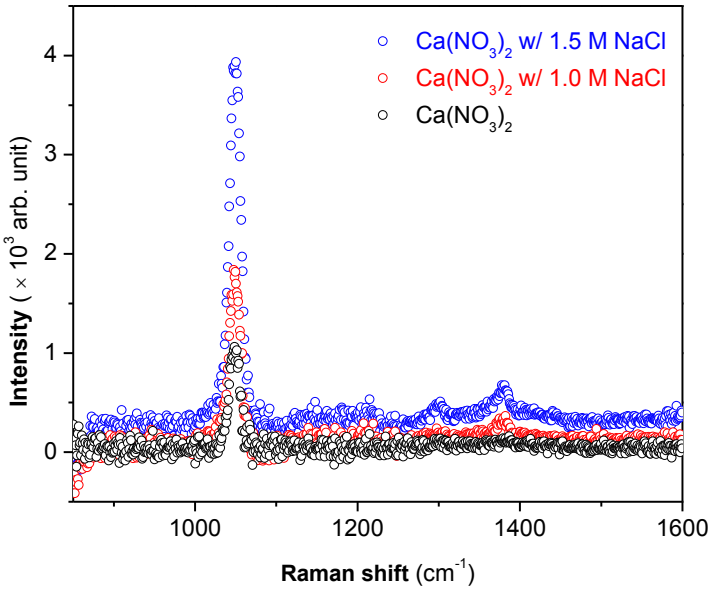

Continued

Figure C1-8. continued

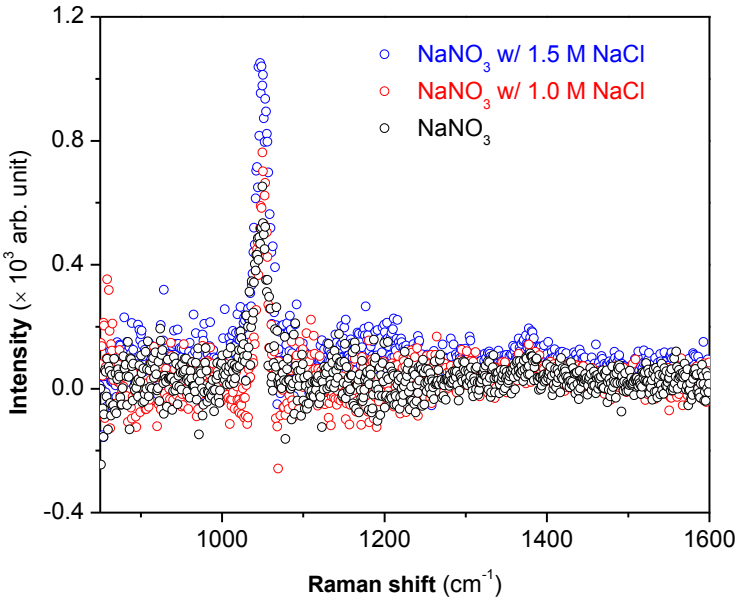

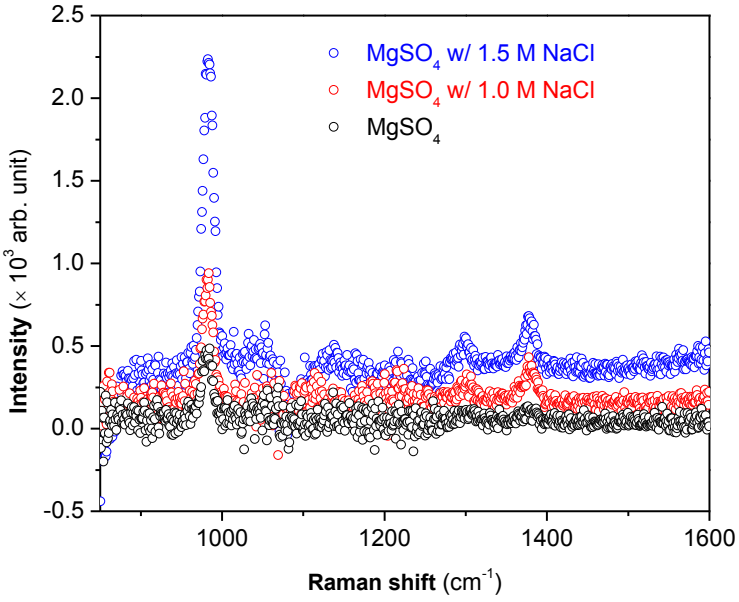

Continued

Figure C1-8. continued